

Astrocyte morphogenesis requires self-recognition

<https://doi.org/10.1038/s41586-025-09013-y>

Received: 6 February 2024

Accepted: 11 April 2025

Published online: 28 May 2025

 Check for updates

John H. Lee^{1,11}✉, Alina P. Sergeeva^{2,11}, Göran Ahlsén³, Seetha Manepalli³, Fabiana Bahna³, Kerry M. Goodman³, Runzhe Xu⁴, Baljit S. Khakh^{5,6}, Joshua A. Weiner^{7,8}, Lawrence Shapiro^{3,9}, Barry Honig^{2,3,9,10} & S. Lawrence Zipursky⁴✉

Self-recognition is a fundamental cellular process across evolution and forms the basis of neuronal self-avoidance^{1–4}. Clustered protocadherin (cPcdh) proteins, which comprise a large family of isoform-specific homophilic recognition molecules, have a pivotal role in the neuronal self-avoidance that is required for mammalian brain development^{5–7}. The probabilistic expression of different cPcdh isoforms confers unique identities on neurons and forms the basis for neuronal processes to discriminate between self and non-self^{5,6,8}. Whether this self-recognition mechanism also exists in astrocytes remains unknown. Here we report that γC3, a specific isoform in the Pcdhy family, is enriched in human and mouse astrocytes. Using genetic manipulation, we demonstrate that γC3 acts autonomously to regulate astrocyte morphogenesis in the mouse visual cortex. To determine whether γC3 proteins act by promoting recognition between processes of the same astrocyte, we generated pairs of γC3 chimeric proteins that are capable of heterophilic binding to each other, but incapable of homophilic binding. Co-expression of complementary heterophilic binding isoform pairs in the same γC3-null astrocyte restored normal morphology. By contrast, chimeric γC3 proteins individually expressed in single γC3-null mutant astrocytes did not. These data establish that self-recognition mediated by γC3 contributes to astrocyte development in the mammalian brain.

A remarkable feature of the interactions that underlie cellular morphogenesis in the brain, particularly the interactions between cellular processes, is how cells discriminate between the many different processes encountered in the developing neuropil. In the mammalian central nervous system (CNS), neurites of different neurons discriminate between their own processes and those of other neurons, in part, through the use of proteins of the cPcdh family. This large family of proteins regulates cell morphology and pattern neural circuits in various ways, including via dendritogenesis, cell survival and synapse formation^{4,5,7–11}. In many neuronal types, cPcdh proteins confer upon neurons the ability to discriminate between self neurites and non-self neurites and to promote self-avoidance, the tendency of processes of the same cells to avoid each other, thus promoting uniform coverage of receptive fields and preventing inappropriate self-synapses or autapses¹². cPcdh genes encode 50–60 single-pass transmembrane domain proteins and are organized into three linked clusters: *Pcdha*, *Pcdhb* and *Pcdhg*^{13,14} (Fig. 1a). Each isoform exhibits isoform-specific homophilic *trans* binding and is proposed to trigger a repulsive response between processes^{7,15}.

For cPcdh proteins to mediate discrimination between self and non-self, neurons must also express different isoforms^{4,5,7}. This is

achieved through the probabilistic expression of multiple cPcdh isoforms in each neuron^{4–6}. This endows each neuron with a unique tag, allowing neurites from the same cell to bind to each other, which, in turn, is proposed to activate repulsion, preventing them from associating with each other. Different cPcdh isoforms from any of the three clusters heterodimerize in *cis* in the plane of the plasma membrane, promoting *trans* interactions between processes that express the same combination of isoforms, but not between those that express different combinations^{6,16,17}. As non-self processes all have different combinations of isoforms, mismatches prevent interactions between partially matching sets of cPcdh proteins on opposing membranes^{6,16}. This *cis*-mediated mechanism has a key role in regulating specificity of self-recognition. It does so by limiting the size of *trans* complexes formed between cPcdh complexes on opposing membranes of cells expressing different combinations of cPcdh proteins.

In the course of analysing transcriptomic data from the cortex^{18–20}, we found that γC3 is preferentially expressed at high levels in mature astrocytes in both mice and humans (Fig. 1b–d). Although neurons, oligodendrocytes and microglia in mice also express γC3, they do so at much lower levels and also express other isoforms^{5,21–23} (Fig. 1b). In mouse, γC3 is the most highly expressed cPcdh isoform in astrocytes

¹Department of Psychiatry and Biobehavioral Sciences, University of California Los Angeles, Los Angeles, CA, USA. ²Department of Systems Biology, Columbia University, New York, NY, USA.

³Zuckerman Mind Brain and Behavior Institute, Columbia University, New York, NY, USA. ⁴Department of Biological Chemistry, University of California Los Angeles, Los Angeles, CA, USA.

⁵Department of Physiology, University of California Los Angeles, Los Angeles, CA, USA. ⁶Department of Neurobiology, University of California Los Angeles, Los Angeles, CA, USA. ⁷Iowa Neuroscience Institute, The University of Iowa, Iowa City, IA, USA. ⁸Department of Biology, The University of Iowa, Iowa City, IA, USA. ⁹Department of Biochemistry and Molecular Biophysics, Columbia University, New York, NY, USA. ¹⁰Department of Medicine, Columbia University, New York, NY, USA. ¹¹These authors contributed equally: John H. Lee, Alina P. Sergeeva.

✉e-mail: JohnHLee@mednet.ucla.edu; lzipursky@mednet.ucla.edu

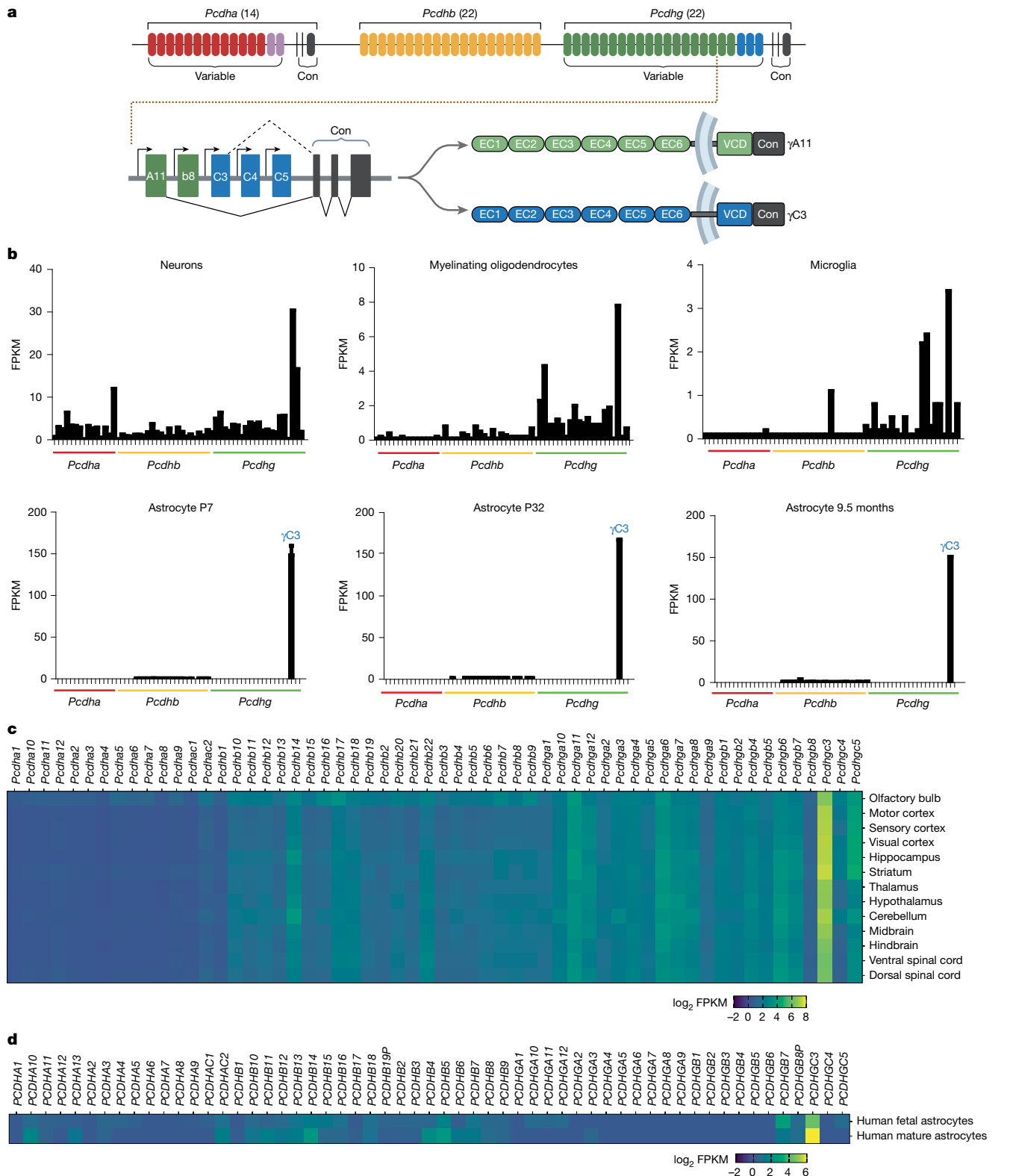


Fig. 1 | γ C3 is the predominant cPcdh isoform in mouse and human astrocytes.

a, The mouse cPcdh gene cluster contains an array of 58 exons, each encoding different extracellular, transmembrane, and proximal cytoplasmic domains. The α and γ proteins share common exons encoding a terminal segment of the cytoplasmic domain, referred to as the constant domain (Con), which is encoded by three exons. Each α and γ variable exon also encodes a short, isoform-specific cytoplasmic region immediately following the transmembrane domain, known as the variable cytoplasmic domain (VCD). Each β protein comprises a distinct C-terminal segment encoded entirely by each variable exon. **b**, Transcriptional profiling from RNA sequencing of cPcdh genes from the mouse cerebral cortex

in neurons, oligodendrocytes and microglia at P7 (top row) and at three stages of development in astrocytes (bottom row) from the same region. Note the difference in the scale on the y-axis between the top and bottom rows. The data are from Zhang et al.¹⁸, Clarke et al.²⁰ and <https://brainrnaseq.org/>. FPKM, fragments per kilobase of exon per million mapped fragments. **c**, Expression of cPcdh genes in astrocytes from different regions of the mouse central nervous system. The data are from Endo et al.²⁴ and <http://astrocyternaseq.com/>. **d**, RNA-sequencing data for human astrocytes immunopanned from fetal (18–18.5 weeks of gestation) and adult human brains. The data are from Zhang et al.¹⁹ and <https://brainrnaseq.org/>. Heat maps show \log_2 FPKM values for the cPcdh cluster genes.

across 13 different brain regions²⁴ (Fig. 1c and Supplementary Table 1). Thus, whereas most neurons express different combinations of cPcdh isoforms in a largely probabilistic fashion^{5,6}, astrocytes preferentially express γ C3 at high levels in both mouse and human. This marked difference in the mode of expression of γ C3 and its conservation between mouse and human led us to assess the role of γ C3 in the developing mouse visual cortex.

γ C3 is required for astrocyte morphogenesis

We first sought to determine the consequence of γ C3 loss in mice that lacked γ C3 in all cell types²⁵. γ C3-knockout (KO) mice were viable and fertile and exhibited no gross signs of developmental abnormalities or neuronal cell death²⁵. To explore the role of γ C3 in astrocytes we sparsely labelled them by injection of PHP.eB adeno-associated viruses (AAVs) into the retro-orbital sinus of neonatal mice at postnatal day 1 (P1) (Fig. 2a). This virus, which encodes a membrane-targeted GFP (Lck-GFP) driven by an astrocyte-specific sequence (GfaABC₁D^{26,27}), labels astrocytes throughout the brain^{24,28} (Extended Data Fig. 1a). Viral delivery at P1 resulted in robust astrocyte-specific Lck-GFP expression in the visual cortex at P8, which persisted through later developmental stages (Extended Data Fig. 1b).

We examined the development of wild-type and γ C3-null mutant astrocytes in fixed thick tissue preparations of primary visual cortex (V1) using confocal microscopy. We used the fast optical tissue clearing protocol²⁹ to efficiently clear thick tissues (Supplementary Fig. 1), which enabled us to assess overall shape and approximate volume of astrocytes, and compared these features in different genetic backgrounds. Astrocyte processes typically undergo extensive branching^{30–32} between P8 and P21 (Fig. 2b). Mutant astrocytes displayed altered morphology at all stages of development, including reduced territory size and apparent volume (Fig. 2b–d). These phenotypes were reminiscent of altered morphology in mutant axon terminals and dendrites of several neuron types^{5,7,33}.

To examine whether γ C3 exhibits layer-specific expression, we used quantitative *in situ* hybridization to quantify γ C3 transcripts at the single-cell level. We found that γ C3 is expressed by all *Slc1a3* (also known as GLAST)-positive astrocytes, consistent with γ C3 having a role shared by all cortical astrocytes (Extended Data Fig. 2a,b). We did not detect a significant difference in γ C3 expression between upper and lower layers. As our analysis of published gene expression profiling shows that γ C3 is the predominant cPcdh isoform expressed in astrocytes across brain regions (Fig. 1), we also examined astrocyte morphology in the hippocampus of γ C3-KO mice and, consistent with observations in the visual cortex, found reduced territory size and apparent volume (Extended Data Fig. 3a–c).

In wild-type mice, neighbouring astrocytes exhibit minimal overlap, effectively tiling the entire CNS³². We set out to assess whether, in addition to regulating astrocyte morphology, γ C3 mediates interactions between neighbouring astrocytes to promote tiling. To distinguish between processes of different astrocytes at the boundaries between them, we utilized a multicolour imaging approach similar to Multicolor FlpOut in *Drosophila*³⁴. We constructed a panel of viruses expressing a spaghetti-monster fluorescent protein (smFPs), each modified with an array of small peptide epitopes to enable robust immunolabelling with commercially available tag-specific antibodies³⁵. To enhance the labelling of fine astrocyte processes, an N-terminal membrane targeting sequence was fused to the smFP proteins enabling their targeting to the plasma membrane. Mixtures of three different viruses were injected into the retro-orbital sinus giving rise to a multicoloured array of astrocytes, clearly delineating minimal overlap at cell boundaries (Extended Data Fig. 4a,b). We measured the overlapping surface volumes between neighbouring astrocyte processes and calculated the percentage of overlap by dividing the overlapping volume by the whole cell volume (Extended Data Fig. 4c and Methods). Deletion of γ C3 did not lead to

altered overlap in the processes of neighbouring astrocytes (Extended Data Fig. 4d,e), indicating that astrocyte tiling does not require the γ C3 isoform.

γ C3 is required cell-autonomously in astrocytes

We next sought to assess whether γ C3 acts autonomously to regulate astrocyte morphology. To do this, we selectively removed the entire Pcdhg cluster from astrocytes using the Cre–LoxP method regulated temporally by tamoxifen and assessed morphology with and without co-expression of a γ C3 cDNA in these cells (Fig. 3a). We carried out control experiments to demonstrate the following: (1) effective removal of the Pcdhg cluster selectively from astrocytes; and (2) targeted expression of γ C3 in an astrocyte-specific, Cre-dependent manner from the *ROSA26* locus in mice in which the Pcdhg cluster was removed (Extended Data Figs. 5 and 6). These methods provide a proxy for measuring Pcdhg and γ C3 protein levels^{7,36–38}.

The astrocyte phenotypes associated with the removal of the Pcdhy cluster selectively from astrocytes in early postnatal life (P1–P3) were similar to those observed in γ C3-KO mice (Fig. 3b,c). Furthermore, targeted expression of γ C3 in an astrocyte-specific, Cre-dependent manner from the *ROSA26* locus in these mutant astrocytes rescued the phenotype on a Pcdhg-null mutant background (Fig. 3b,c; genotypes are presented in Methods). These data indicate that γ C3 is required in astrocytes for normal morphogenesis.

To determine whether γ C3 is required only in astrocytes for their normal development, we used a viral gene delivery strategy to selectively restore γ C3 expression in astrocytes in γ C3-KO mice that lacked γ C3 in all cell types. We generated an AAV construct encoding a full-length γ C3 cDNA fused with a C-terminal 3×V5 tag (γ C3FL) (Fig. 4a) under the control of the astrocyte-specific GfaABC₁D promoter and co-injected this into retro-orbital sinus with a virus to visualize astrocyte morphology. Sparsely distributed γ C3-mutant astrocytes expressed γ C3FL and this rescued the mutant phenotype (Fig. 4d,e; detected with the anti-V5 antibody; Extended Data Fig. 7a). That is, γ C3 expression in a single astrocyte surrounded by γ C3-null mutant cells (neurons, astrocytes and other glial cells) significantly rescues the phenotype.

Thus, expression of γ C3 molecules in astrocytes is both necessary and sufficient for astrocyte morphogenesis. Furthermore, although γ C3 is required in astrocytes, it is required in a strictly cell-autonomous fashion; there is no requirement for interactions between γ C3 proteins on neighbouring astrocytes.

γ C3 mutants lacking homophilic binding do not rescue astrocyte morphology in γ C3 mutants

If homophilic binding is required for γ C3 function in astrocytes, the mutant phenotypes that we observed, along with prior work in several neuronal cell types^{6–8,15,33}, suggests that γ C3 may promote interactions between processes of the same astrocyte. It is possible, however, that γ C3 recognizes a different, yet to be identified, protein on the surface of astrocytes that is embedded in the extracellular matrix or on the surface of other cortical cell types that regulate astrocyte morphogenesis. If this were the case, in the simplest interpretation, point mutations that disrupt homophilic binding would not be expected to disrupt astrocyte morphogenesis.

To test this, we designed two single-point mutations in γ C3 that were predicted to disrupt homophilic binding (Fig. 4a–c). cPcdh proteins form *trans*-dimer interfaces with their N-terminal EC1–EC4 extracellular domains binding in an anti-parallel orientation^{6,16,39}. Both the EC1::EC4 and EC2::EC3 interfaces must be formed for binding to occur. To disrupt binding we designed two mutants in which the hydrophobic residues Leu87 and Leu342, which are buried within the EC1::EC4 interface, were replaced with negatively charged glutamate (Fig. 4c). Both mutant

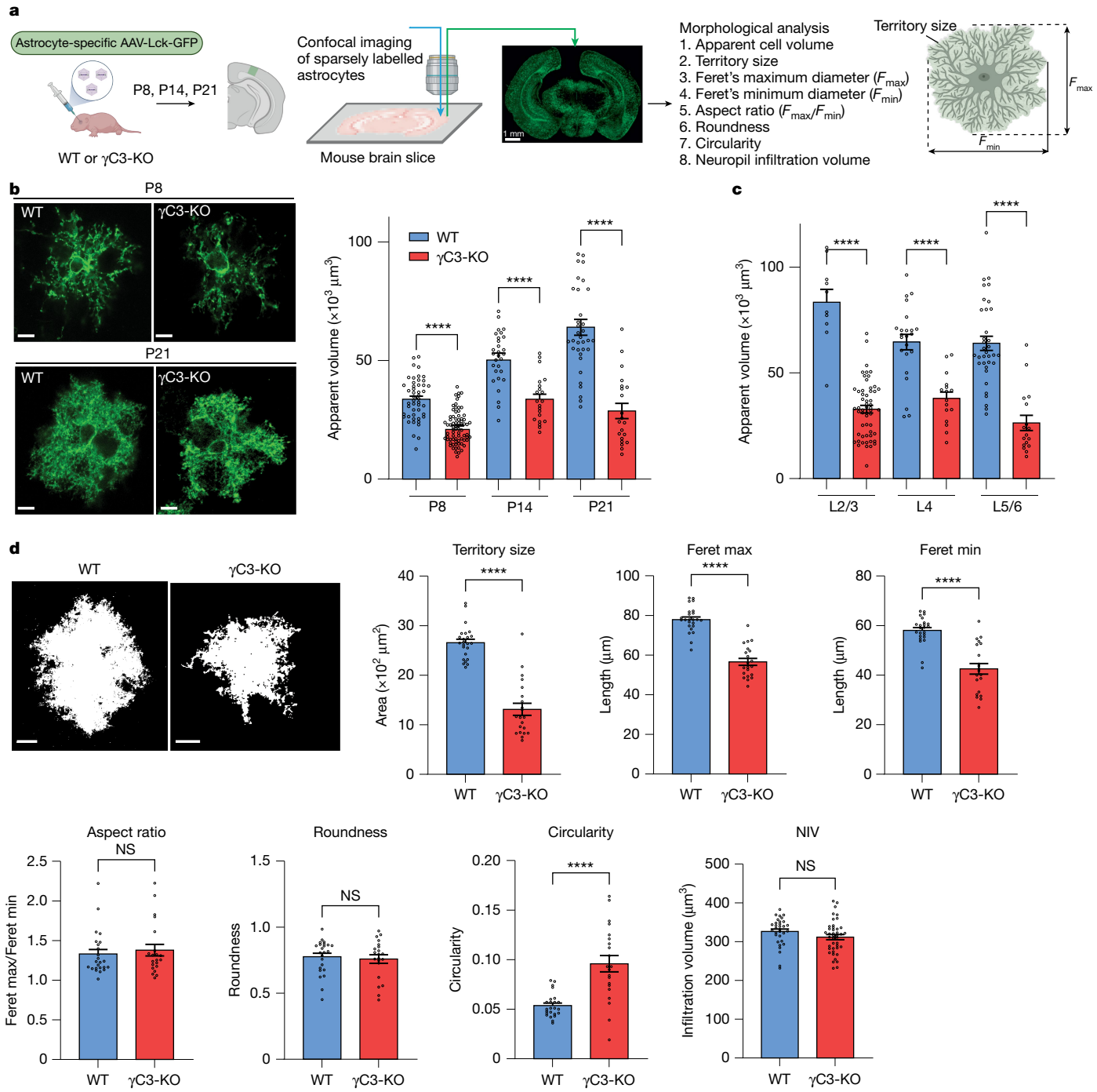


Fig. 2 | Astrocyte morphology is disrupted in γ C3-KO mice. **a**, AAV vectors expressing Lck-GFP (myristoylated GFP that localizes to the cytoplasmic face of the plasma membrane), controlled by an astrocyte-specific promoter were retro-orbitally injected into P1 neonates. Astrocyte morphology analysed using multiple metrics (Methods). WT, wild type. **b**, Astrocyte morphology in wild-type and γ C3-KO mutants. Quantification of apparent volumes of astrocytes (Methods). Astrocytes in L6 showed reduced volumes from P8 to P21 in γ C3-KO mice. P8: wild type ($n = 48$ astrocytes from 3 mice) and γ C3-KO ($n = 75$ astrocytes from 3 mice); P14: wild type ($n = 29$ astrocytes from 3 mice) and γ C3-KO ($n = 21$ astrocytes from 3 mice); P21: wild type ($n = 35$ astrocytes from 6 mice) and γ C3-KO ($n = 21$ astrocytes from 6 mice). Two-sided unpaired *t*-test with Welch's correction was used for comparisons. **c**, Astrocytes in P21 wild-type and γ C3-KO mice. Wild type: L2/3, $n = 10$; L4, $n = 23$; and L5/6, $n = 35$

astrocytes each from six mice. γ C3-KO: L2/3, $n = 56$; L4, $n = 16$; and L5/6, $n = 17$ astrocytes each from 6 mice. Two-sided unpaired *t*-test with Welch's correction was used for comparisons across cortical layers (L2/3, L4 and L5/6). **d**, Astrocyte morphology analysed with multiple morphological metrics. Representative images of single astrocytes flattened in a confocal volume from both wild-type and γ C3-KO mice in layer 5/6 V1 mice. The results are summarized in plots representing various morphological parameters. Wild type, $n = 24$ astrocytes from six mice; γ C3-KO, $n = 21$ astrocytes from 4 mice. For neuropil infiltration volume (NIV; Methods): wild type, $n = 32$ cells from 3 mice; γ C3-KO, $n = 42$ cells from 3 mice. Error bars represent s.e.m. Two-sided unpaired *t*-test with Welch's correction. Nested analysis was performed for all statistical comparisons to confirm the results; details are provided in Supplementary Table 4. Scale bars, 10 μm . *** $P < 0.001$, **** $P < 0.0001$; NS, not significant.

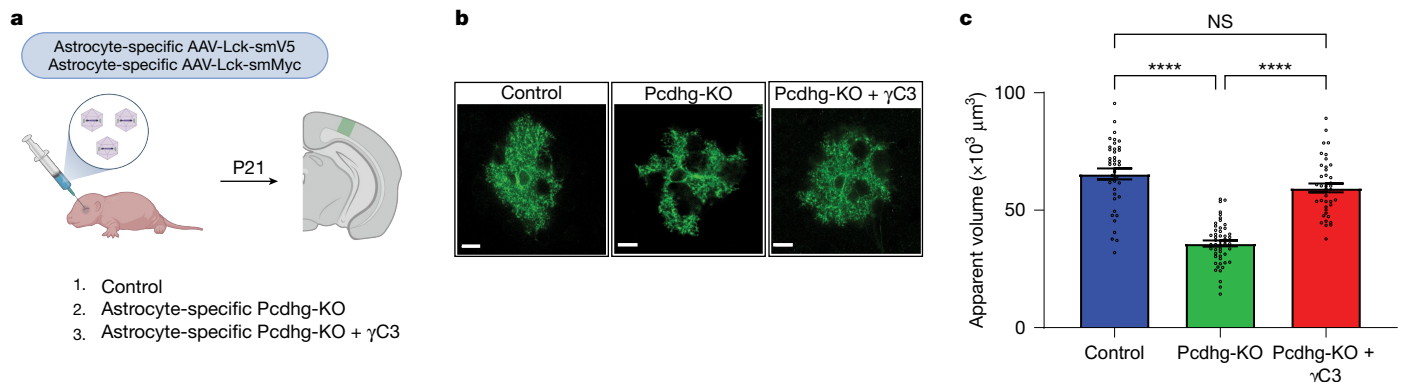


Fig. 3 | Replacement of the Pcdhg cluster with a single isoform rescues astrocyte morphology.

a, Strategy to determine whether a single isoform alone is sufficient for normal astrocyte morphology. Mice were injected with two AAVs each expressing a different membrane marker (Lck-smV5 or Lck-smMYC) under the astrocyte-specific GfaABC₁D promoter to label astrocyte morphology. Using two different labelled viruses enabled delineation of boundaries between adjacent astrocytes. **b,c**, Fluorescence microscopy (**b**) and quantification of astrocyte volume (**c**) show that astrocytes lacking the Pcdhg complex exhibit

marked defects in morphology. The expression of γC3 in Pcdhg-deficient astrocytes (Methods) substantially rescues astrocyte morphological defects. See Methods for genetic scheme. Morphological differences were analysed using one-way ANOVA with post hoc Tukey's tests for pairwise comparisons. Specific *P* values are provided in Supplementary Table 4. Control: *n* = 40 cells from 3 mice; Pcdhg-KO, *n* = 50 cells from three mice; Pcdhg-KO + γC3, *n* = 40 cells from 3 mice. Error bars represent s.e.m. Scale bars, 10 μm. Nested analysis was performed to confirm the results; details are provided in Supplementary Table 4.

protein fragments (γC3 EC1–EC4 L87E and γC3 EC1–EC4 L342E) were monomers, as determined by analytical ultracentrifugation (AUC) (Fig. 4b). We incorporated these single-point mutations into full-length γC3 proteins modified with a C-terminal 3×V5 epitope (Fig. 4a). These constructs were introduced virally via retro-orbital injection to transduce the cortical astrocytes of γC3-KO mice at P1 and the phenotypes were assessed at P21 (Extended Data Fig. 7b,c). In contrast to wild-type γC3, neither γC3(L87E) nor γC3(L342E) rescued the γC3-null phenotype; the astrocytes transduced with these constructs exhibited altered morphology that was indistinguishable from that of γC3-null mutants (Fig. 4d,e). We interpret these data as indicating a requirement for γC3 to mediate interactions between processes of the same astrocytes through homophilic interactions.

Interactions between γC3 in the same astrocyte are required for astrocyte morphogenesis

It remains possible that mutations that abrogate homophilic interactions may also prevent mutant forms of γC3 from binding to a different ligand. Thus, to critically assess whether γC3 binding between processes of the same cell is required for astrocyte morphogenesis, we designed non-identical pairs of γC3 variants that bind to each other, but not to themselves, and tested their ability to rescue the γC3-mutant phenotype when expressed alone or together in the same mutant astrocyte (Fig. 5). That is, we converted γC3 homophilic binding into heterophilic binding. We used a similar strategy previously to demonstrate that Dscam1 isoforms in *Drosophila* promote interactions between processes of the same neuron⁴⁰.

Our approach was based, in large part, on the design of chimeras formed by combining domains of γC3 with those of either γC4 or γC5 (Extended Data Fig. 8 and Supplementary Fig. 2). Swapping two domains of γC3 (blue) with two domains from γC4 (green) yielded chimeras that were monomeric in solution (Fig. 5a and Extended Data Fig. 8b for M1; and the other chimera generated in the swap shown in Extended Data Fig. 8c and Supplementary Table 2). On the basis of interactions between complementary domains alone, we would have expected these chimeras to bind to each other (that is, heterophilically), but they did not (Extended Data Fig. 8d).

We thus set out to modify their interfaces with amino acid substitutions to selectively promote heterophilic binding. This required introduction of multiple mutations into prospective heterophilic

pairs guided by reiterative testing, visual inspection and computational analysis. The detailed approach used to generate these pairs is described in Methods (Extended Data Fig. 8 and 9, Supplementary Fig. 3 and Supplementary Table 3). Two different chimeric pairs exhibited heterophilic binding, concomitant with the loss of homophilic binding. The M1::M6 and M3::M8 pairs of the EC1–EC4 *trans*-binding domain fragments had dissociation constant (*K*_d) values of 32 μM and 80 μM, respectively (Fig. 5b and Supplementary Table 2). These *K*_d estimates are in the range of most cell adhesion molecules and are stronger than the *K*_d for γC3 (115 μM).

We next sought to assess whether the γC3-mutant astrocyte phenotypes were rescued by co-expression of heterophilic binding pairs. We incorporated the M1, M3, M6 and M8 EC1–EC4 chimeras into full-length γC3 protein variants. Each chimera was also tagged with a C-terminal 3×HA or 3×V5 epitope (Fig. 5a) to assess expression *in vivo* using antibody staining (Fig. 5c). These chimeras were expressed using the astrocyte-specific GfaABC₁D promoter and incorporated into AAVs for *in vivo* expression. At P1, γC3-KO mice received injections of either a single chimera (M1, M3, M6 or M8) or a complementary pair of chimeras (M1::M6 or M3::M8 pairs) (Fig. 5d and Methods). Only astrocytes that exhibited positive staining for the epitope tags—indicating correct expression—were analysed. Single chimeric proteins lacking the ability to form homodimers did not rescue the astrocyte morphology phenotype (Fig. 5d). By contrast, heterophilic binding partners (M1::M6 or M3::M8), when introduced as pairs, significantly rescued the phenotype (Fig. 5d, e).

One consideration in these experiments is that it is not possible to accurately quantify the expression of different chimeric proteins. Furthermore, studies in a variety of cell types indicate that only a small fraction of the cPcdh proteins are trafficked to the plasma membrane (that is, most remains intracellular)^{17,25,41,42}. Thus, it is unclear how the increase in viral load of different chimeric constructs relates to protein levels at the cell surface. Although it is possible that the rescue that we see with complementary pairs of chimeras reflects increased protein levels, this seems unlikely. First, none of the four chimeras show any evidence of rescue individually (Fig. 5d). Second, homophilic binding of chimeras was not measurable *in vitro* (Fig. 5b). Finally, significant rescue of astrocyte morphology was observed only following co-infection of heterophilic binding pairs (Fig. 5d).

In summary, the rescue results with chimeric cPcdh molecules, together with other genetic experiments in this study, provide strong

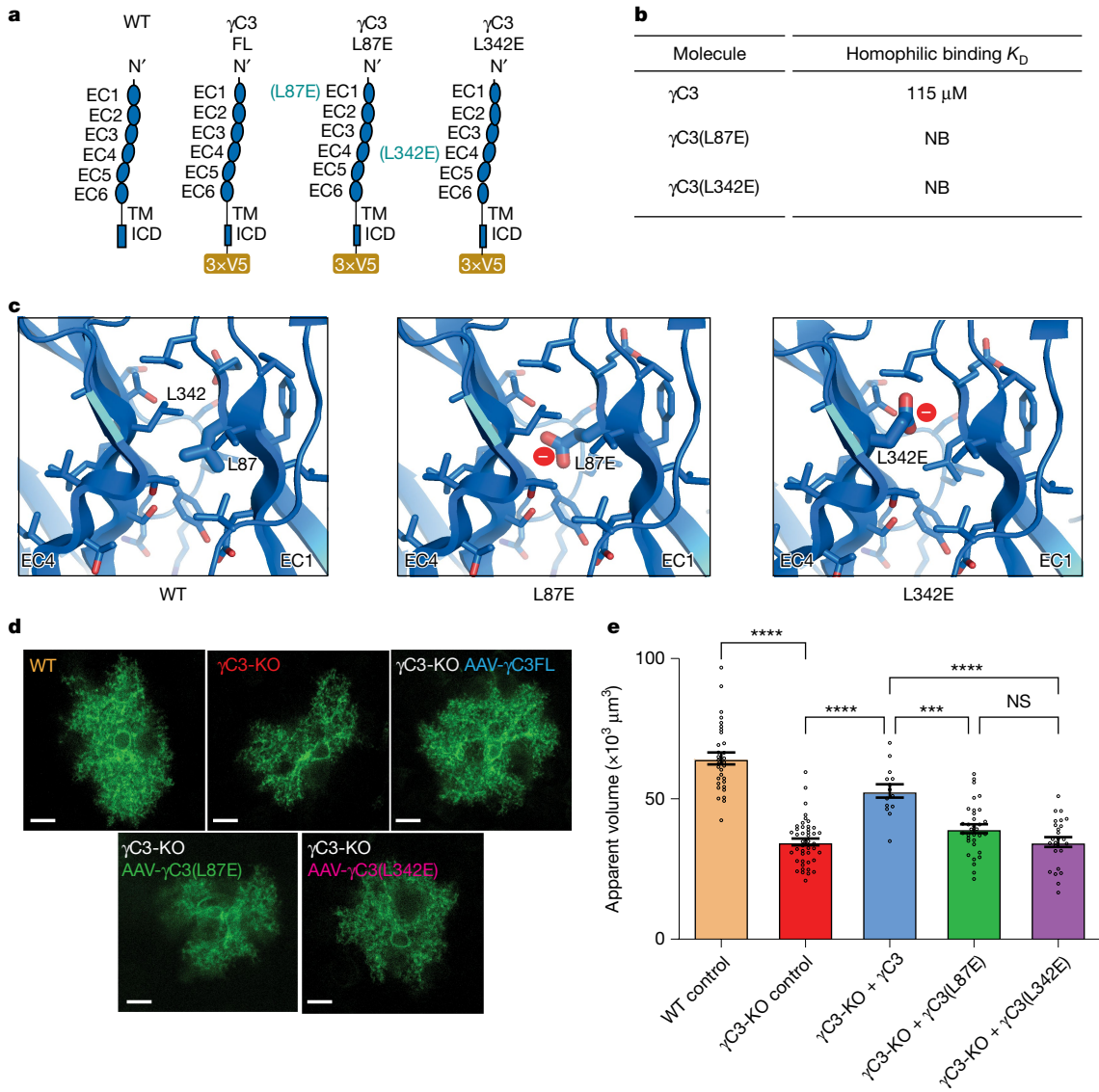


Fig. 4 | γC3 homophilic recognition specificity is required for astrocyte morphology. **a**, Schematic of proteins tested for rescue in wild-type and γC3-KO mice. **b**, Summary of AUC experiments on the EC1–EC4 wild-type and mutant proteins. NB, no measurable binding. **c**, Structure-based design of mutations that disrupt homophilic binding. Unsatisfied buried charges (red spheres) disrupt homophilic binding. **d,e**, Rescue experiments using AAVs to express different γC3 constructs under the control of the astrocyte-specific GfaABC₁D promoter in wild-type and γC3-KO mutants in layer 6 of V1.

Morphological differences were analysed using one-way ANOVA with post hoc Tukey's tests for pairwise comparisons. Wild type, $n = 32$ cells from 3 mice; γC3-KO control, $n = 45$ cells from 5 mice; γC3-KO + γC3FL, $n = 14$ cells from 5 mice; γC3-KO + γC3(L87E), $n = 33$ cells from 5 mice; and γC3-KO + γC3(L342E), $n = 25$ cells from 5 mice. Error bars represent s.e.m. Scale bars, 10 μm. Nested analysis was performed to confirm the results; details are provided in Supplementary Table 4.

evidence that homophilic binding between γC3 proteins in the same astrocyte promotes normal astrocyte morphology during development.

Discussion

The γC3 isoform from the Pcdhy cluster is preferentially expressed at high levels in both mouse and human astrocytes during development. We show through genetic studies that γC3 is necessary for astrocyte morphogenesis, is required in astrocytes but not neurons for this function, and that re-expression of γC3 in γC3-KO mice is sufficient to rescue the astrocyte mutant morphology phenotype. Through the analysis of mutant isoforms of γC3 with altered binding specificities, we provide evidence that normal astrocyte development relies on γC3 homophilic interactions between processes of the same cell (Extended Data Fig. 10). That is, γC3 is required for astrocyte self-recognition.

The expression of γC3 in human astrocytes suggests that this function is evolutionarily conserved.

Establishing that γC3 mediates interactions between processes of the same astrocyte relied on generating γC3 mutants in which homophilic binding was converted to heterophilic binding. The primary challenge in generating these mutants was that different isoforms of Pcdhy form *trans* dimers with rather distinct structures, precluding simply achieving heterophilic specificity by combining different domains. Indeed, there are marked variations in surface interactions of cPcdh proteins (for example, resulting in substantial deviations up to 4.5 Å root mean squared deviation (rmsd))⁴³. Our analysis predicted that the EC2–EC3 orientation in the γC3 *trans* dimer is different than that of γC4, which affects the contacts in the interface. By contrast, γC5 is expected to align closely with the orientation of γC4. To accommodate these differences, we successfully created heterophilic recognition molecules

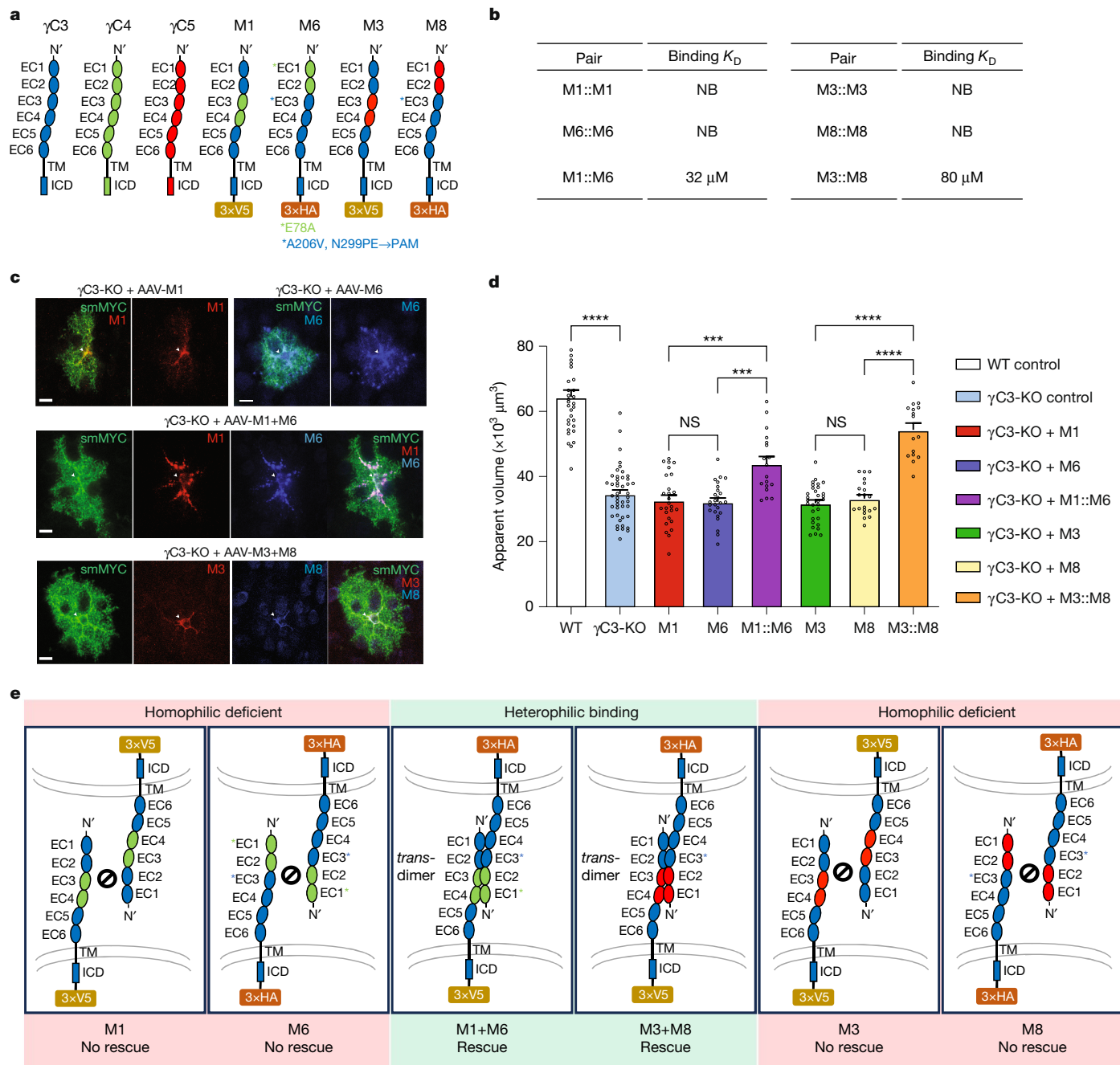


Fig. 5 | Complementary chimeras expressed in astrocytes only rescue the morphology defect in γC3 -null mutant astrocytes. **a**, Schematic showing protein constructs used in rescue experiments. **b**, K_D values for EC1–EC4 fragments of chimeras shown in **a**, as determined using AUC. **c**, Astrocytes transduced with virus-expressed chimeras under the control of the astrocyte-specific GfaABC₁D promoter were identified by staining using antibodies to the epitope tags (arrowheads). Weak signal to noise was often observed with HA antibody. Astrocyte morphology was visualized using anti-MYC staining to visualize AAV-Lck-smMyc. **d**, Quantification of apparent volumes of astrocytes

for different genotypes as indicated. Morphological differences were analysed using one-way ANOVA with post hoc Tukey's tests for pairwise comparisons. Wild type, $n = 32$ cells in 3 mice; γC3 -KO control, $n = 45$ cells in 5 mice; M1, $n = 26$ cells in 5 mice; M6, $n = 25$ cells in 5 mice; M1::M6, $n = 18$ cells in 5 mice; M3, $n = 31$ cells in 5 mice; M8, $n = 20$ cells in 5 mice; M3::M8: $n = 16$ cells in 5 mice. Error bars represent s.e.m. **e**, The schematic shows that complementary pairs of chimeras (M1::M6 or M3::M8) enable heterophilic binding within the same astrocytes. Scale bars, 10 μm . Nested analysis was performed to confirm the results; details are provided in Supplementary Table 4.

by introducing targeted mutations to force the modelled chimeras to adapt *trans*-dimer structures analogous to γC4 . The ability of these complementary chimeras to rescue supports the notion that during development interactions between γC3 expressed in the same cell is necessary to promote normal astrocyte morphogenesis.

The complexity of astrocyte morphology poses a challenge to understanding how γC3 -mediated self-recognition regulates morphogenesis mechanistically. The simplest interpretation of our morphological

characterization is that γC3 promotes process outgrowth. At a mechanistic level, it may do so in different ways, and here we suggest two alternatives. γC3 binding may promote repulsion of processes away from each other and thus, indirectly, promote outgrowth into new neuropil territory. This is analogous to the role of clustered Pcdhy isoforms in regulating self-avoidance in starburst amacrine cells^{7,15}. Alternatively, transient binding between γC3 on opposing membranes of processes of the same astrocyte may directly activate cytoskeletal

dynamics promoting process outgrowth. As the cytoplasmic domain of γ C3 is unique among cPcdh proteins in its binding to Axin1²⁵, which engages Cdc42, a key regulator of cytoskeletal remodelling⁴⁴, engagement of this signalling complex by γ C3 may directly promote process outgrowth. Like many other cell surface guidance and recognition molecules, γ C3 may function in an adhesive or repulsive way in a context-dependent fashion. Future experiments will be necessary to uncover the mechanistic details by which self-recognition contributes to astrocyte morphogenesis.

In principle, astrocytes could also use γ C3 to promote recognition between neighbouring astrocytes, minimizing overlap between them, and thus promoting tiling of astrocytes throughout the CNS. Wild-type astrocytes tile the CNS exhibiting minimal overlap. Deletion of γ C3 did not alter the overlap between adjacent astrocytes. Thus, the simplest interpretation is that γ C3 does not regulate tiling. Tiling may be regulated by different sets of recognition molecules at the astrocyte–astrocyte interface or alternatively other molecules may act in a redundant fashion with γ C3 to regulate this process.

In contrast to the cell-type-enriched expression of γ C3 in astrocytes, the probabilistic expression of cPcdh isoforms occurs in most neurons. Consequently, each cell acquires a unique identity and this, in turn, enables neurites to distinguish between sister neurites (that is, neurites of the same cell) from those of other neurons. It is generally believed that this leads to self-avoidance, allowing neurites to uniformly cover receptive fields and prevent interactions (for example, formation of autapses) between them^{5–7}.

We suggest three possible reasons why astrocytes preferentially use γ C3 rather than adopting the probabilistic expression of different isoforms as neurons do. First, as the processes of adjacent astrocytes do not share territory (in contrast to the extensive intermingling of neuronal processes), astrocytes must discriminate between their own processes and the processes of a multitude of neuron types, but not other astrocytes. Selective enrichment of γ C3 may be sufficient to provide this specificity. Second, astrocytes express very high levels of γ C3 transcripts. This high level of expression may be necessary to support interactions between the vast number of astrocyte processes. Finally, as the γ C3 sequences in the juxtamembrane domain are different from other Pcdh isoforms, these may promote interactions between astrocyte-specific proteins, which act together to pattern astrocyte morphology—either through distinct complexes on the cell surface or the activation of distinct intracellular signalling pathways. Previous studies demonstrated that a specific isoform encoded by the *Pcdha* gene complex, *PcdhaC2*, is selectively expressed in serotonergic neurons and promotes axon tiling⁸, providing additional evidence that different isoforms may have evolved distinct functions. The prominent role of cPcdh family members in many cell types (such as astrocytes and different neuron types) to promote self-non-self discrimination, and the use of some isoforms in cell-type-specific ways is similar to the diverse roles of different Dscam proteins in *Drosophila* neurodevelopment^{40,45–49}.

In summary, the expression of γ C3 isoforms in mouse and human astrocytes and the function that we describe here for γ C3 to regulate mouse astrocyte morphology indicate a conserved role for this isoform in regulating astrocyte development.

Online content

Any methods, additional references, Nature Portfolio reporting summaries, source data, extended data, supplementary information, acknowledgements, peer review information; details of author contributions and competing interests; and statements of data and code availability are available at <https://doi.org/10.1038/s41586-025-09013-y>.

1. Hattori, D. et al. Robust discrimination between self and non-self neurites requires thousands of *Dscam1* isoforms. *Nature* **461**, 644–648 (2009).

2. Miura, S. K., Martins, A., Zhang, K. X., Graveley, B. R. & Zipursky, S. L. Probabilistic splicing of *Dscam1* establishes identity at the level of single neurons. *Cell* **155**, 1166–1177 (2013).
3. Zipursky, S. L. & Grueber, W. B. The molecular basis of self-avoidance. *Annu. Rev. Neurosci.* **36**, 547–568 (2013).
4. Sanes, J. R. & Zipursky, S. L. Synaptic specificity, recognition molecules, and assembly of neural circuits. *Cell* **181**, 1434–1435 (2020).
5. Mountoufaris, G. et al. Multicluster Pcdh diversity is required for mouse olfactory neural circuit assembly. *Science* **356**, 411–414 (2017).
6. Thu, C. A. et al. Single-cell identity generated by combinatorial homophilic interactions between α , β , and γ protocadherins. *Cell* **158**, 1045–1059 (2014).
7. Lefebvre, J. L., Kostadinov, D., Chen, W. V., Maniatis, T. & Sanes, J. R. Protocadherins mediate dendritic self-avoidance in the mammalian nervous system. *Nature* **488**, 517–521 (2012).
8. Chen, W. V. et al. *Pcdhac2* is required for axonal tiling and assembly of serotonergic circuitries in mice. *Science* **356**, 406–411 (2017).
9. Meltzer, S. et al. γ -Protocadherins control synapse formation and peripheral branching of touch sensory neurons. *Neuron* **111**, 1776–1794.e1710 (2023).
10. Garrett, A. M. et al. CRISPR/Cas9 interrogation of the mouse *Pcdhg* gene cluster reveals a crucial isoform-specific role for *Pcdhg4*. *PLoS Genet.* **15**, e1008554 (2019).
11. Mancia Leon, W. R. et al. Clustered γ -protocadherins regulate cortical interneuron programmed cell death. *eLife* **9**, e55374 (2020).
12. Sanes, J. R. & Zipursky, S. L. Synaptic specificity, recognition molecules, and assembly of neural circuits. *Cell* **181**, 536–556 (2020).
13. Zipursky, S. L. & Sanes, J. R. Chemoaffinity revisited: dscams, protocadherins, and neural circuit assembly. *Cell* **143**, 343–353 (2010).
14. Wu, Q. & Maniatis, T. A striking organization of a large family of human neural cadherin-like cell adhesion genes. *Cell* **97**, 779–790 (1999).
15. Ing-Esteves, S. & Lefebvre, J. L. γ -Protocadherins regulate dendrite self-recognition and dynamics to drive self-avoidance. *Curr. Biol.* **34**, 4224–4239.e4 (2024).
16. Rubinstein, R. et al. Molecular logic of neuronal self-recognition through protocadherin domain interactions. *Cell* **163**, 629–642 (2015).
17. Schreiner, D. & Weiner, J. A. Combinatorial homophilic interaction between γ -protocadherin multimers greatly expands the molecular diversity of cell adhesion. *Proc. Natl. Acad. Sci. USA* **107**, 14893–14898 (2010).
18. Zhang, Y. et al. An RNA-sequencing transcriptome and splicing database of glia, neurons, and vascular cells of the cerebral cortex. *J. Neurosci.* **34**, 11929–11947 (2014).
19. Zhang, Y. et al. Purification and characterization of progenitor and mature human astrocytes reveals transcriptional and functional differences with mouse. *Neuron* **89**, 37–53 (2016).
20. Clarke, L. E. et al. Normal aging induces A1-like astrocyte reactivity. *Proc. Natl. Acad. Sci. USA* **115**, E1896–E1905 (2018).
21. Esumi, S. et al. Monoallelic yet combinatorial expression of variable exons of the protocadherin- α gene cluster in single neurons. *Nat. Genet.* **37**, 171–176 (2005).
22. Kaneko, R. et al. Allelic gene regulation of *Pcdh- α* and *Pcdh- γ* clusters involving both monoallelic and biallelic expression in single Purkinje cells. *J. Biol. Chem.* **281**, 30551–30560 (2006).
23. Toyoda, S. et al. Developmental epigenetic modification regulates stochastic expression of clustered protocadherin genes, generating single neuron diversity. *Neuron* **82**, 94–108 (2014).
24. Endo, F. et al. Molecular basis of astrocyte diversity and morphology across the CNS in health and disease. *Science* **378**, eadc9020 (2022).
25. Steffen, D. M. et al. A unique role for protocadherin γ C3 in promoting dendrite arborization through an Axin1-dependent mechanism. *J. Neurosci.* **43**, 918–935 (2023).
26. Shigetomi, E. et al. Imaging calcium microdomains within entire astrocyte territories and endfeet with GCaMPs expressed using adeno-associated viruses. *J. Gen. Physiol.* **141**, 633–647 (2013).
27. Shigetomi, E., Kracun, S., Sofroniew, M. V. & Khakh, B. S. A genetically targeted optical sensor to monitor calcium signals in astrocyte processes. *Nat. Neurosci.* **13**, 759–766 (2010).
28. Gangwani, M. R. et al. Neuronal and astrocytic contributions to Huntington’s disease dissected with zinc finger protein transcriptional repressors. *Cell Rep.* **42**, 111953 (2023).
29. Zhu, X. et al. Ultrafast optical clearing method for three-dimensional imaging with cellular resolution. *Proc. Natl. Acad. Sci. USA* **116**, 11480–11489 (2019).
30. Clavreul, S. et al. Cortical astrocytes develop in a plastic manner at both clonal and cellular levels. *Nat. Commun.* **10**, 4884 (2019).
31. Ge, W. P., Miyawaki, A., Gage, F. H., Jan, Y. N. & Jan, L. Y. Local generation of glia is a major astrocyte source in postnatal cortex. *Nature* **484**, 376–380 (2012).
32. Bushong, E. A., Martone, M. E. & Ellisman, M. H. Maturation of astrocyte morphology and the establishment of astrocyte domains during postnatal hippocampal development. *Int. J. Dev. Neurosci.* **22**, 73–86 (2004).
33. Molumby, M. J., Keeler, A. B. & Weiner, J. A. Homophilic protocadherin cell–cell interactions promote dendrite complexity. *Cell Rep.* **15**, 1037–1050 (2016).
34. Nern, A., Pfeiffer, B. D. & Rubin, G. M. Optimized tools for multicolor stochastic labeling reveal diverse stereotyped cell arrangements in the fly visual system. *Proc. Natl. Acad. Sci. USA* **112**, E2967–E2976 (2015).
35. Viswanathan, S. et al. High-performance probes for light and electron microscopy. *Nat. Methods* **12**, 568–576 (2015).
36. Lefebvre, J. L., Zhang, Y., Meister, M., Wang, X. & Sanes, J. R. γ -Protocadherins regulate neuronal survival but are dispensable for circuit formation in retina. *Development* **135**, 4141–4151 (2008).
37. Garrett, A. M., Schreiner, D., Lobas, M. A. & Weiner, J. A. γ -Protocadherins control cortical dendrite arborization by regulating the activity of a FAK/PKC/MARCKS signalling pathway. *Neuron* **74**, 269–276 (2012).
38. Garrett, A. M. & Weiner, J. A. Control of CNS synapse development by γ -protocadherin-mediated astrocyte–neuron contact. *J. Neurosci.* **29**, 11723–11731 (2009).

Article

39. Goodman, K. M. et al. Structural basis of diverse homophilic recognition by clustered α- and β-protocadherins. *Neuron* **90**, 709–723 (2016).
40. Wu, W., Ahlsen, G., Baker, D., Shapiro, L. & Zipursky, S. L. Complementary chimeric isoforms reveal Dscam1 binding specificity *in vivo*. *Neuron* **74**, 261–268 (2012).
41. Fernandez-Monreal, M. et al. γ-protocadherins are enriched and transported in specialized vesicles associated with the secretory pathway in neurons. *Eur. J. Neurosci.* **32**, 921–931 (2010).
42. O’Leary, R. et al. A variable cytoplasmic domain segment is necessary for gamma-protocadherin trafficking and tubulation in the endosome/lysosome pathway. *Mol. Biol. Cell* **22**, 4362–4372 (2011).
43. Goodman, K. M. et al. How clustered protocadherin binding specificity is tuned for neuronal self-/nonself-recognition. *eLife* **11**, e72416 (2022).
44. Chen, Y. et al. Axin regulates dendritic spine morphogenesis through Cdc42-dependent signaling. *PLoS ONE* **10**, e0133115 (2015).
45. Tadros, W. et al. Dscam proteins direct dendritic targeting through adhesion. *Neuron* **89**, 480–493 (2016).
46. Millard, S. S., Flanagan, J. J., Pappu, K. S., Wu, W. & Zipursky, S. L. Dscam2 mediates axonal tiling in the *Drosophila* visual system. *Nature* **447**, 720–724 (2007).
47. Millard, S. S., Lu, Z., Zipursky, S. L. & Meinertzhagen, I. A. *Drosophila* Dscam proteins regulate postsynaptic specificity at multiple-contact synapses. *Neuron* **67**, 761–768 (2010).
48. Matthews, B. J. et al. Dendrite self-avoidance is controlled by Dscam. *Cell* **129**, 593–604 (2007).
49. Wojtowicz, W. M., Flanagan, J. J., Millard, S. S., Zipursky, S. L. & Clemens, J. C. Alternative splicing of *Drosophila* Dscam generates axon guidance receptors that exhibit isoform-specific homophilic binding. *Cell* **118**, 619–633 (2004).

Publisher’s note Springer Nature remains neutral with regard to jurisdictional claims in published maps and institutional affiliations.

Springer Nature or its licensor (e.g. a society or other partner) holds exclusive rights to this article under a publishing agreement with the author(s) or other rightsholder(s); author self-archiving of the accepted manuscript version of this article is solely governed by the terms of such publishing agreement and applicable law.

© The Author(s), under exclusive licence to Springer Nature Limited 2025

Methods

Mice

Mouse breeding and husbandry procedures were conducted in strict accordance with the guidelines and approval of UCLA's Animal Care and Use Committee at the University of California, Los Angeles and were supervised by J. Trachtenberg. Mice were provided with food and water ad libitum and were maintained under a 12 h:12 h day:night cycle, with a maximum of 4 adult mice per cage. The PcdhyC3-knockout (γ C3-KO) mice were generated and previously characterized by the laboratories of J. Weiner and R. W. Burgess²⁵ (The Jackson Laboratory). The *Pcdhy*^{fcon3/fcon3} transgenic mice have been described previously⁵⁰. Additionally, the ROSA26-CAG::lox-Stop-lox-PcdhyC3-mCherry mice were originally generated by J. Lefebvre and J. Sanes⁷. The *Aldh1l1*-CreERT2 (ref. 51) (IMSR_JAX:031008) and ROSA26-LSL-Cas9-P2A-eGFP⁵² (IMSR_JAX:026175) mice were obtained from The Jackson Laboratory.

Tamoxifen induction for Cre mice

Tamoxifen (Sigma) was freshly prepared at a concentration of 20 mg ml⁻¹ in corn oil and allowed to dissolve overnight at 37 °C with continuous agitation. To induce gene expression, mice were injected with 5 mg kg⁻¹ tamoxifen (Sigma T5648) dissolved in corn oil on postnatal day 1 for three consecutive days. *Aldh1l1*-creERT2 × *Pcdhg*^{fcon3/fcon3}, *Aldh1l1*-creERT2 × *Pcdhg*^{fcon3/fcon3} × ROSA26-CAG::lox-Stop-lox-PcdhgC3-mCherry and *Aldh1l1*-creERT2 × ROSA26-LSL-Cas9-P2A-eGFP were used for tamoxifen injections.

Whole-mount tissue optical clearing

To achieve optical clearing of brain tissues, we used the fast optical clearing method (FOCM). The FOCM reagent was prepared as a solution containing 30% (w/v) urea, 20% (w/v) D-sorbitol and 5% glycerol dissolved in DMSO (D8418). Mice designated for histological analysis were anaesthetised with isoflurane and then transcardially perfused with ice-cold 1× PBS, followed by 4% paraformaldehyde in 1× PBS buffer. Brains were subsequently removed, postfixed in 4% paraformaldehyde overnight, and transferred to a 30% sucrose 1× PBS solution for a minimum of 48 h at 4 °C. Sections 200 µm in thickness were cryosectioned using a Leica cryostat microtome. These sections were washed three times for 1 h in 1× PBS, followed by permeabilization and blocking for 4 h in a solution containing 0.3% Triton X-100 and 10% normal goat serum (NGS), 1% BSA and 0.5% Triton X-100 in 1× PBS. Subsequently, slides were incubated with primary antibodies diluted in 3% NGS, 1% BSA and 0.5% Triton X-100 in 1× PBS for 72 h at 37 °C. Primary antibodies were used at the following concentrations: Rabbit anti-V5 (Bethyl, 1:500), Chicken anti-V5 (Bethyl, 1:500), MYC rat antibody (Bio-Rad, 1:500), Anti-GFP antibody (abcam, 1:1,000), anti-NeuN (Millipore, 1:500), anti-Kir4.1 antibody (Alomone Labs, 1:500). After 6× washes of 6 h with 1× PBS, tissues were incubated with Alexa Fluor 488, 568 and 647 secondary antibodies (Invitrogen, 1:500). When necessary, tissues were treated with a nuclear counterstain, either DAPI (Invitrogen, 1:1,000) or NeuroTrace Green (Invitrogen, 1:500), for 48 h at 37 °C. Finally, tissues were washed 6× for 4 h with 1× PBS and mounted on glass slides using a holder. The holder was filled with FOCM reagent, and the brain section was incubated for 15 min. Once the tissues became optically cleared, a glass coverslip was placed on the holder and sealed with nail polish for imaging.

Plasmids and AAVs

To generate GfaABC_iD-Lck-smV5 and Lck-smMyc plasmids, cytosolic smFP-V5 and smFP-Myc cDNAs were amplified by PCR from the pCAG-smFP-V5 (Addgene #59758) and pCAG-smFP-Myc plasmid (Addgene #59757). The pCAG-smFP-V5 and pCAG-smFP-Myc plasmids were provided by L. Looger. The GfaABC_iD-Lck-GFP plasmid (Addgene #61099) was digested with restriction enzyme using Xhol and Sall. PCR amplified smFP-V5 and smFP-Myc sequences were annealed into the cleavage sites of the plasmid backbone using T4 ligase to generate

GfaABC_iD-Lck-smV5 and Lck-smMyc plasmids, respectively. The cDNAs of the full-length γ C3 fused with C-terminal 3×V5 epitopes was synthesized by Genewiz Priority Gene (Azenta Life Science). Next, the gene fragments were cut with restriction enzymes to facilitate cloning into the Xhol and XbaI digested GfaABC_iD-Lck-GFP plasmid backbone to generate AAV-GfaABC_iD- γ C3FL construct. To generate the heterophilic binding deficient AAV chimera constructs, the EC1–EC4 domains of the wild-type full-length γ C3 was replaced with the EC1–EC4 domains of the modified γ C3 heterophilic binding chimeras (M1, M3, M6 and M8). To enable in vivo detection of the expressed constructs, 3×V5 tags were added to the C terminus of the M1 and M3 constructs, and 3×HA tags were fused to the C terminus of the M6 and M8 constructs. The cDNAs for the M1, M3, M6 and M8 constructs were synthesized by Genewiz Priority Gene (Azenta Life Science). The synthesized gene fragments were restriction digested and cloned into the AAV-GfaABC_iD-Lck-GFP plasmid backbone to generate AAV-GfaABC_iD-M1, AAV-GfaABC_iD-M3, AAV-GfaABC_iD-M6 and AAV-GfaABC_iD-M8 constructs.

Generation of γ C3 single-point mutants

Two γ C3 single-point mutants, γ C3(L87E) and γ C3(L342E), were designed by introducing an unsatisfied negative charge at the EC1:EC4 interface of the γ C3 homodimer (Fig. 4c). The biophysical characteristics of these homophilic binding deficient mutants were then assessed in the context of the γ C3 EC1–EC4 construct (Supplementary Table 2). QuickChange site-directed mutagenesis kit from Stratagene was used to introduce point mutations on the full-length γ C3 cDNA with fused C-terminal 3×V5 tags following the mutagenesis PCR protocol. The resulting AAV-GfaABC1D- γ C3(L87E) and AAV-GfaABC1D- γ C3(L342E) constructs were verified by sequencing.

AAV production and administration

Neonatal mice were gently removed from their holding cages and positioned on their side. Sterile saline and a cotton-tipped applicator were used to clean the injection site. A 33-gauge needle attached to the Hamilton microinjection syringe was inserted at a 45° angle into the left retro-bulbar sinus of the neonatal mice. A total injection volume of 10 µl virus diluted in 1× PBS was delivered into the retro-orbital bulbar sinus. After viral injection, mild pressure was applied at the injection site to minimize backflow of the injected viruses. AAVs were administered at an approximate viral titre of 1×10¹¹ viral genomes per mouse. All injections were performed on P1 or P2. Mice were euthanized at designated time points in accordance with approved animal protocols and procedures.

To assess the effects of homophilic binding deficient mutants, separate litters of wild-type and γ C3-KO mice each received AAV-GfaABC_iD- γ C3FL, AAV-GfaABC_iD- γ C3(L87E), or AAV-GfaABC_iD- γ C3(L342E). All groups were also injected with AAV-GfaABC_iD-Lck-smMyc to label astrocyte morphology. In the heterophilic binding chimera experiment, the litter of γ C3-KO mice was equally divided to evaluate the effect of each heterophilic binding pair. To evaluate the phenotypic effect of the M1+M6 heterophilic binding chimera, the litters were equally divided to receive either AAV-GfaABC_iD-M1, AAV-GfaABC_iD-M6 or AAV-GfaABC_iD-M1 + AAV-GfaABC_iD-M6 constructs. Following a similar experimental design, other γ C3-KO litters were equally divided to receive AAV-GfaABC_iD-M3, AAV-GfaABC_iD-M8 and AAV-GfaABC_iD-M3+M8 treatments to evaluate the effect of M3 and M8 heterophilic binding pairs on astrocyte morphology. The same wild-type and γ C3-KO control groups are shown in Figs. 4e and 5d. All AAV viruses were produced by the Janelia Viral Vector Core. Viral titres were measured using PCR with reverse transcription (RT-PCR) to quantify the viral particle concentration in the final virus preparations.

Confocal imaging and morphology analysis

Confocal images were acquired using a Zeiss LSM 880 confocal microscope equipped with Zen digital imaging software. Imaging was performed at magnifications of 10× (NA 0.45), 20× (NA 0.8) and 40× (NA 1.2)

Article

glycerol immersion objectives (Zeiss), with each image frame consisting of $1,024 \times 1,024$ pixels. *z*-Stack images were collected for each astrocyte with a step size of $0.5\text{ }\mu\text{m}$ between *z*-planes. The astrocyte morphology was labelled with AAV expressing membrane-tagged fluorescent reporters (Lck-GFP, Lck-smMYC and Lck-smV5), which allowed labelling of the cell membrane and visualization of cell shape and fine astrocyte branches. Only astrocytes that could be fully imaged in their entirety were selected for analysis. Any cells that overlapped with others or extended beyond the imaging boundaries were excluded from the analysis. The ZEN file format from the confocal microscope was converted into the IMARIS file format using the Imaris File Converter tool, which includes a built-in deconvolution function. The images were then imported into IMARIS 10.01 software (Bitplane) for volume reconstruction. Background subtraction was applied to reduce noise. A region of interest (ROI) was manually defined to encapsulate the entire single astrocyte to minimize background signal interference. For surface reconstruction, the membrane-tagged fluorescent reporter channel was selected as the source channel. The intensity threshold for the membrane-tagged signal was manually set by adjusting the intensity curve. Each cell was visually inspected to confirm accurate thresholding, ensuring complete reconstruction of the astrocyte surface. Each surface was then filtered by volume to eliminate any small surfaces generated by background fluorescence. The generated functional surface was used to calculate morphometric parameters, including the apparent cell volume of individual astrocytes. We chose to use the term 'apparent volume' to indicate that the volume measurement is an approximation, since light microscopy cannot resolve the finer astrocyte processes, which are at the scale of 50 nm. Throughout all imaging sessions, key acquisition parameters, such as detector gain, exposure time and pinhole size, were maintained consistently across experiments. Laser power was carefully adjusted within a controlled range to optimize signal detection while preventing oversaturation and minimizing photobleaching. The fluorescence intensities of the GFP or smFPs used to image astrocyte morphology were comparable across all experimental groups. For 2D morphological analysis, various morphology parameters, such as Feret max, Feret min, aspect ratio, territory size, roundness and circularity, were performed in accordance with established protocols^{24,53}. This assessment was carried out using maximum intensity projections, and each morphological parameter was quantified using ImageJ software.

Astrocyte tiling analysis

For the analysis of astrocyte tiling, astrocyte morphology was labelled with a mixture of AAVs containing the astrocyte-specific promoter (*GfaABC1D*) that drives the expression of membrane-tagged reporters (Lck-GFP, Lck-smMYC and Lck-smV5), which allowed multicolour labelling and visualization of astrocyte processes and delineated the points of contact at the boundaries between adjacent cells. Brains from wild-type and γ C3-KO mice were collected at P21. Two-hundred micrometre brain sections were processed to increase the likelihood of capturing the entirety of individual astrocytes. The apparent cell volume for individual astrocytes was reconstructed using IMARIS software (Bitplane), following the surface and volume reconstruction protocol described above. The co-localization tool in IMARIS was used to generate a co-localization channel for the regions in which the masked fluorescent channels overlapped. The co-localization surface was then reconstructed to calculate the overlapping volume between adjacent astrocytes. The astrocyte tiling index was determined by dividing the overlapping co-localization volume by the apparent cell volume of the individual astrocytes. This ratio measures the percentage of tiling between neighbouring astrocytes.

Neuropil infiltration analysis

To quantify the degree of astrocyte infiltration into the neuropil, *z*-stack images were captured at $40\times$ magnification from Lck-GFP-,

Lck-smMYC- or Lck-smV5-labelled astrocytes in $200\text{-}\mu\text{m}$ brain sections. Astrocytes expressing the fluorescent label located in layer 6 of the visual cortex were selected for analysis. For each astrocyte, three ROIs, each measuring $10\text{ }\mu\text{m} \times 10\text{ }\mu\text{m} \times 10\text{ }\mu\text{m}$, were selected within the neuropil, excluding regions containing cell bodies, major branches, or endfeet. These ROIs were reconstructed using the surface tool in Imaris software. The surface volume for each ROI was calculated, and the three values from each astrocyte were averaged to derive a mean neuropil infiltration volume per astrocyte. The number of mice and the number of cells analysed per mouse is provided in the figure legends for each experiment.

EASI-FISH method

Tissue preparation. Tissue preparation: Tissue fixation and preparation: Fixed frozen brain slices were sectioned at $100\mu\text{m}$ thickness and stored in 70% ethanol at 4°C . The primary visual cortex (V1Sp) was micro-dissected referencing to coordinates from Franklin and Paxino, 2012. Multiple sections per mouse were used for experiment and analysis. All sections were cut into rectangle shapes ($3 \times 4\text{ mm}$) for easier orientation and optimal imaging. All tissue handling steps were done in RNase-free condition.

EASI-FISH procedure. Experimental procedures were closely followed by a previously established protocol for expansion-assisted iterative fluorescence *in situ* hybridization (EASI-FISH)⁵⁴ with a few exceptions. Tissue slices were rehydrated in PBS at room temperature ($2 \times 15\text{ min}$) and incubated in MOPS buffer (20 mM, pH 7.7, 30 min). Tissue was incubated overnight (37° C) in MOPS buffer with 1 mg ml^{-1} MelphaX and 0.1 mg ml^{-1} Acryloyl-X, SE for RNA crosslinking. The gelation and probe hybridization steps were as stated in a previously established protocol⁵⁴. Probes targeting mCherry, eGFP and *Slc1a3* were used at $1\text{ }\mu\text{M}$ concentration in hybridization buffer. For hybridization chain reaction, hairpins were used at $3\text{ }\mu\text{M}$ concentration (conjugated to AF488, AF546, and AF594) in amplification buffer. Tissue gel was not digested with DNase1 for visualization of nuclei.

Image acquisition and sample handling. Before imaging, samples were stained in 1:1,000 dilution of $5\text{ }\mu\text{g ml}^{-1}$ DAPI ($2 \times 30\text{ min}$). Samples were mounted to a poly-L-lysine-coated glass coverslip that was glued to a customized plastic holder. Samples were equilibrated in imaging chamber with 1× PBS for at least 2 h before imaging acquisition. All samples were imaged on a Zeiss Lightsheet LS7 selective plane illumination microscope. A $20\times$ water-immersion objective ($20\times/1.0\text{ W}$ Plan-Apochromat Corr DIC M27 75 mm, refractive index = 1.33) was used for imaging with 1× zoom. Multiple imaging fields of view were acquired for each tissue section at $0.23\text{ }\mu\text{m} \times 0.23\text{ }\mu\text{m}$ pixel resolution (post-expansion) and $0.42\text{ }\mu\text{m}$ *z*-step size with dual camera detection of two channels in each camera.

RNA puncta quantification. An experimenter blinded to the genotype of the mice analysed the sections. Astrocytes were identified using the astrocyte-specific marker *Slc1a3*, detected as RNA puncta through a fluorescently labelled RNA probe. These puncta were then used to segment astrocyte cell boundaries. GFP or mCherry RNA puncta were visualized with fluorescently labelled probes, enabling the identification of individual RNA molecules within astrocytes. The number of GFP or mCherry RNA puncta per astrocyte was quantified using a co-localization criterion, in which only puncta clearly overlapping with DAPI-stained nuclei and residing within *Slc1a3*-positive regions were included in the analysis. The results were reported as the total number of RNA puncta per astrocyte, stratified by genotype.

RNAscope image processing and quantification

RNAscope was performed according to a previously published protocol⁵⁵. All image stacks were projected along the *z*-axis for downstream

imaging processing. CellProfiler was used to perform nuclear and cell segmentation, as well as FISH puncta counting. Astrocytes were segmented on the basis of *Slc1a3* RNA staining with an additional Gaussian filter referencing previously established protocols⁵⁶. Astrocytes included in the analysis were visually checked to ensure no aberration in segmentation or puncta calling (puncta calling follows Cheng et al.⁵⁵). Data were analysed in R using custom scripts to compare RNA counts (number of puncta per astrocyte) between cortical layers. A Wilcoxon rank-sum test was used for statistical comparison.

Building *trans*-dimer models

We used a crystal structure of γ C4 (Protein Data Bank ID: 7JGZ)⁴³ as a template to build models of *trans* dimers for wild-type γ C3, wild-type γ C5, single-point mutants (to explain their effects on binding; γ C3(L87E), γ C3(L342E) and γ C4(E78A)) and the chimeras ($M_i, i = 1, 2, 3, 6, 8$) designed for exclusive heterophilic binding. Sequences of all modelled EC1–EC4 fragments (residues 1–421, numbering as in Protein Data Bank ID: 7JGZ) are juxtaposed with the template in Supplementary Fig. 3. The multiple sequence alignment shown in Supplementary Fig. 3 was generated with Clustal Omega⁵⁷ and visualized via <https://escript.ibcp.fr/ESPrpt/ESPrpt/>⁵⁸.

The variants were modelled by mutating γ C4 amino acids of the template structure into amino acids of the target proteins using BuildModel utility in FoldX⁵⁹. This method ensures the backbone of the modelled proteins mirrors the template (γ C4), gauging their propensity to form a γ C4-like *trans* dimer. For instance, to build models of γ C3 and γ C5 wild-type *trans* dimers, we made 215 and 194 mutations to each γ C4 protomer within a γ C4:: γ C4 *trans* dimer, yielding $\Delta\Delta G$ values of 27.2 and 5.9 kcal mol⁻¹, respectively. Here, $\Delta\Delta G$ denotes the interaction energy of the *trans* dimer, derived from its total folding energy using the AnalyseComplex utility in FoldX. The chimeras exhibited destabilization in a γ C4-dictated *trans*-dimer conformation by 16–18 kcal mol⁻¹, similar to γ C3. These modelled *trans* dimers and their binding energies relative to γ C4 are shown in Extended Data Fig. 9a. Of note, the figure shows the precursor chimera models corresponding to merging EC1–EC2 (residues 1–205) and EC3–EC4 (residues of 206–421) fragments of γ C3 (blue) with either γ C4 (green) or γ C5 (red). Only M1 and M3 match the precursor chimera in sequence. M_i chimeras (where $i = 2, 6, 8$) carry additional point mutations atop the precursor chimeras, introduced via FoldX to bolster *trans* dimerization (detailed further in ‘Design of chimeras’).

Design of chimeras

Utilizing FoldX, we first modelled heterophilic protocadherin chimeras combining sequences of γ C3 with either γ C4 or γ C5 (refer to ‘Building *trans*-dimer models’). Subsequent mutations were introduced to correct the non-complementary surfaces. Largely positive relative FoldX energies of the initial chimera models (Extended Data Fig. 9a) suggested interface issues that might hinder γ C4-like heterophilic chimera binding. Particularly, the issues were likely from the γ C3 fragments (as γ C3:: γ C3 was most destabilized compared to γ C4:: γ C4; Extended Data Fig. 9a).

By examining all model structures, we identified problematic chemical interactions, especially those between polar or charged and hydrophobic residues. A comparison of these destabilizing contacts with the template interactions revealed specific issues. For instance, Extended Data Fig. 9b shows a ribbon representation of a γ C4 *trans* dimer (template, green) and a model of a γ C3 *trans* dimer (forced to have a backbone identical to γ C4, blue). The amino acids at the EC2–EC3 boundary of γ C4 are mostly hydrophobic (see labelled residues shown as sticks in a diamond-shaped area, shaded in grey) whereas γ C3 has polar/charged residues (N299 and E301, underlined in cyan) that are incompatible with the neighbouring hydrophobic residues (L204, A118 and L117). Furthermore, a hydrophobic contact in a γ C4 dimer formed by two Val residues (V206) was missing in γ C3 (as it has Ala in place of Val). Hence, A206, N299, and E301 residues of γ C3 would probably

destabilize binding in a γ C4-like orientation due to polar-hydrophobic mismatches at the EC2::EC3 interface. This logic extends to chimeras containing γ C3 fragments. Of note, γ C5 interface is similar in chemical composition to that of γ C4 featuring V206 and PAM (299–301) (Extended Data Fig. 9c and Supplementary Fig. 3).

To validate our observations, we employed computational mutagenesis via FoldX. We mutated residues of the precursor chimera models to make the *trans*-dimer interface at the EC2–EC3 boundary more hydrophobic (see details on computational mutagenesis procedure in⁶⁰). Predictions confirmed that A206V, N299P and E301M mutations would stabilize the interface (Supplementary Table 3).

The E78A mutation enhances homophilic binding in γ C4 (ref. 43). The biophysical effect of this mutation is explained in Supplementary Fig. 2. The E78A mutation was introduced to M2 and M6 chimera featuring fragments of γ C4. The N299P and E301M mutations were introduced to M6 and M8 chimeras together with a predicted neutral (Supplementary Table 3) P300A mutation (as a triple NPE→PAM mutation) to minimize the number of cloning events in the chimera generation. The A206V mutation was effectively introduced by a shift in the EC2–EC3 domain boundary (that is, we merged the domains to preserve the Val–Val contact by keeping Val206 of γ C4 or γ C5 and cutting out Ala206 of γ C3; see Supplementary Fig. 3 for the chosen domain boundary between EC1–EC2 and EC3–EC4 fragments in the M_i chimeras). The NPE→PAM mutation differentiates M6 (with) from M2 (without) and M8 (with) from M4 (without), and it is crucial for restoring hydrophobic complementarity at the EC2–EC3 boundary in the heterophilic chimeric *trans* dimers (Extended Data Fig. 9c) as M1::M6 and M3::M8 both formed heterodimers in AUC whereas M1::M2 and M2::M3 did not (Supplementary Table 2).

Sedimentation equilibrium measurements

Experiments were performed in a Beckman XL-A/I analytical ultracentrifuge (Beckman-Coulter), utilizing six-cell centrepieces with straight walls, 12 mm path length and sapphire windows. All proteins were dialysed overnight and then diluted in TRIS 10 mM, NaCl 150 mM, CaCl₂ 3 mM pH 8.0, 250 mM imidazole. Samples were diluted to 1.1, 0.73 and 0.37 mg ml⁻¹ in channels A, B and C, respectively. Dilution buffer was used as blank. All samples were run at four speeds, 11,000, 14,000, 17,000 and 20,000 rpm, at 25 °C. The lowest speed was held for 20 h after which four measuring scans were taken with 1 h interval, the second lowest speed held for 10 h, followed by four scans as above, the third lowest and the highest speed performed identically as the second lowest speed. All measurements were done at 25 °C, and detection was by interference at 675 nm. Solvent density and protein v-bar were determined using the program SednTerp. (Alliance Protein Laboratories) For calculation of dimeric K_d and apparent molecular weight, all useful data were used in a global fit, using the program SedPhat, obtained from National Institute of Health (www.nibib.nih.gov). All measurements are summarized in Supplementary Table 2.

Protein production

cDNA for mouse cPcdh ectodomain fragments, excluding the predicted signal sequence, were cloned into a p α SHP-H mammalian expression vector (from D.J. Leahy, John Hopkins University), modified with the BiP signal peptide (BiP: MKLSLVAAMLLLSAARA) and a C-terminal octahistidine tag. The signal sequence was predicted using the SignalP 4.0 server. Point mutations were introduced into the constructs using the KOD hot start polymerase (Novagen) following the standard Quikchange protocol (Stratagene). The constructs were expressed in suspension-adapted HEK293 Freestyle cells (Invitrogen) in serum-free media using polyethyleneimine as a transfectant (Polysciences). Media was supplemented with 10 mM CaCl₂ 4 h after transfection. Conditioned media was collected 5 days after transfection, and the secreted proteins were purified by nickel affinity chromatography followed by size exclusion chromatography in 10 mM Tris, pH 8.0, 150 mM sodium

Article

chloride, 3 mM calcium chloride, and 250 mM imidazole, pH 8.0. The purified proteins were concentrated to >3 mg ml $^{-1}$ before sedimentation equilibrium AUC experiments.

Statistical analyses

Data are presented as mean \pm s.e.m. along with the individual data points. For comparisons of two groups, unpaired *t*-test with Welch's correction or nested *t*-tests were used, depending on the experimental design. Parametric tests were used for datasets that passed normality tests, while non-parametric tests were applied to datasets that did not meet normality assumptions. For comparisons of more than two groups, one-way ANOVA with post hoc Tukey's multiple comparison tests or nested ANOVA were used to control for the variability between mice. Specific statistical tests and p-values for each figure panel are provided in Supplementary Table 4. Statistical analyses were performed using R 4.0.2 or GraphPad Prism version 10.3.1. In figures, * $P < 0.05$; ** $P < 0.01$; *** $P < 0.001$, **** $P < 0.0001$. In all cases, $P < 0.05$ was considered significant.

Reporting summary

Further information on research design is available in the Nature Portfolio Reporting Summary linked to this article.

Data availability

All data are available in the main text or the supplementary materials. Requests for further information, resources and reagents should be directed to and will be fulfilled by S.L.Z. Source data are provided with this paper.

50. Prasad, T., Wang, X., Gray, P. A. & Weiner, J. A. A differential developmental pattern of spinal interneuron apoptosis during synaptogenesis: insights from genetic analyses of the protocadherin-γ gene cluster. *Development* **135**, 4153–4164 (2008).
51. Srinivasan, R. et al. New transgenic mouse lines for selectively targeting astrocytes and studying calcium signals in astrocyte processes *in situ* and *in vivo*. *Neuron* **92**, 1181–1195 (2016).

52. Platt, R. J. et al. CRISPR-Cas9 knockin mice for genome editing and cancer modeling. *Cell* **159**, 440–455 (2014).
53. Yu, X. et al. Context-specific striatal astrocyte molecular responses are phenotypically exploitable. *Neuron* **108**, 1146–1162.e1110 (2020).
54. Wang, Y. et al. EASI-FISH for thick tissue defines lateral hypothalamus spatio-molecular organization. *Cell* **184**, 6361–6377.e6324 (2022).
55. Cheng, S. et al. Vision-dependent specification of cell types and function in the developing cortex. *Cell* **185**, 311–327.e324 (2022).
56. Bayraktar, O. A. et al. Astrocyte layers in the mammalian cerebral cortex revealed by a single-cell *in situ* transcriptomic map. *Nat. Neurosci.* **23**, 500–509 (2020).
57. Madeira, F. et al. Search and sequence analysis tools services from EMBL-EBI in 2022. *Nucleic Acids Res.* **50**, W276–W279 (2022).
58. Robert, X. & Gouet, P. Deciphering key features in protein structures with the new ENDscript server. *Nucleic Acids Res.* **42**, W320–W324 (2014).
59. Schymkowitz, J. et al. The FoldX web server: an online force field. *Nucleic Acids Res.* **33**, W382–W388 (2005).
60. Sergeeva, A. P. et al. DIP/Dpr interactions and the evolutionary design of specificity in protein families. *Nat. Commun.* **11**, 2125 (2020).

Acknowledgements The authors would like to thank L. Tang, J. Trachtenberg, P. Katsamba and members of the Khakh and Zipursky laboratories for critical feedback; and S. Phillips for providing statistical analysis and consultation for our study. This work was supported by a grant from the W. M. Keck Foundation to S.L.Z., T32 Neurobehavioral Genetics (T32NS048004) training grant (J.H.L.) and NSF grant IOS-2321481 (B.H.). B.S.K. is supported by NS111583.

Author contributions Conceptualization: J.H.L., S.L.Z., A.P.S., L.S. and B.H. Data curation: J.H.L. and A.P.S. Formal analysis: J.H.L., A.P.S., G.A. and R.X. Funding acquisition: S.L.Z. and B.H. Investigation: J.H.L., S.L.Z., A.P.S., G.A. and K.M.G. Methodology: J.H.L., S.L.Z., B.S.K., J.A.W., A.P.S. and R.X. Project administration: J.H.L. and A.P.S. Resources: S.L.Z., B.S.K., J.A.W., L.S. and B.H. Software: J.H.L. and A.P.S. Supervision: S.L.Z., B.S.K., J.A.W., L.S. and B.H. Validation: J.H.L., G.A., S.M., F.B., K.M.G. and R.X. Visualization: J.H.L. and A.P.S. Writing, original draft: J.H.L., S.L.Z., A.P.S. and B.H. Writing, reviewing and editing: J.H.L., S.L.Z., B.S.K., J.A.W., A.P.S., L.S. and B.H.

Competing interests The authors declare no competing interests.

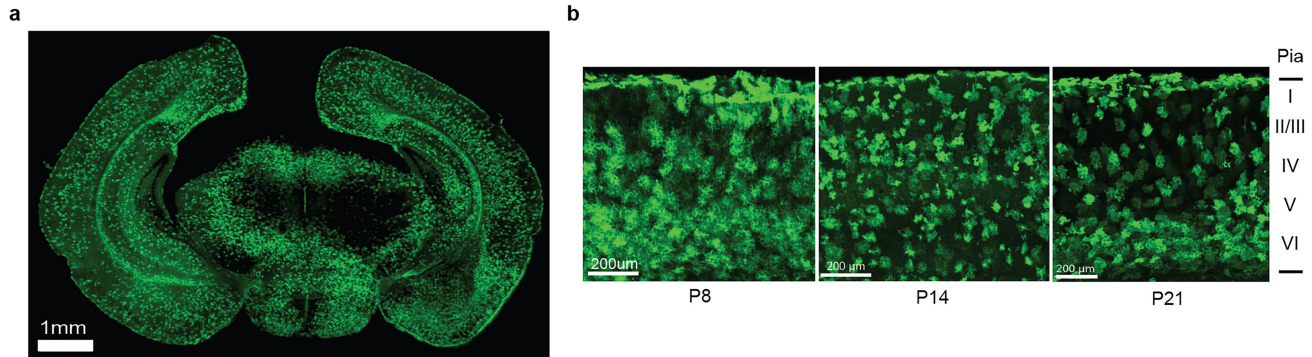
Additional information

Supplementary information The online version contains supplementary material available at <https://doi.org/10.1038/s41586-025-09013-y>.

Correspondence and requests for materials should be addressed to John H. Lee or S. Lawrence Zipursky.

Peer review information *Nature* thanks Daniele Canzio and the other, anonymous, reviewer(s) for their contribution to the peer review of this work.

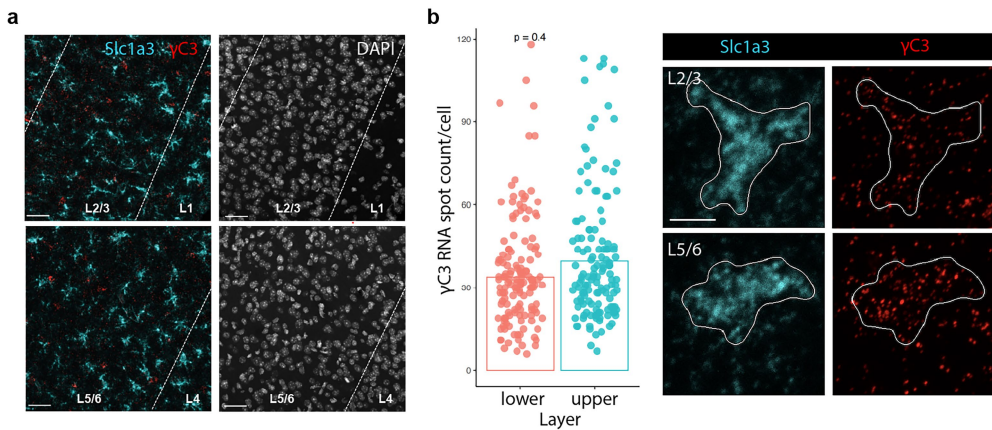
Reprints and permissions information is available at <http://www.nature.com/reprints>.



Extended Data Fig. 1 | Efficient labeling of cortical astrocytes using AAV.

a, Sparse labeling of astrocytes across all cortical layers (P14 mouse brain). AAV.PhP.eB expressing Lck-GFP, under the control of an astrocyte-specific promoter (*GfaABC,D*), which were retro-orbitally injected into neonates at P1.

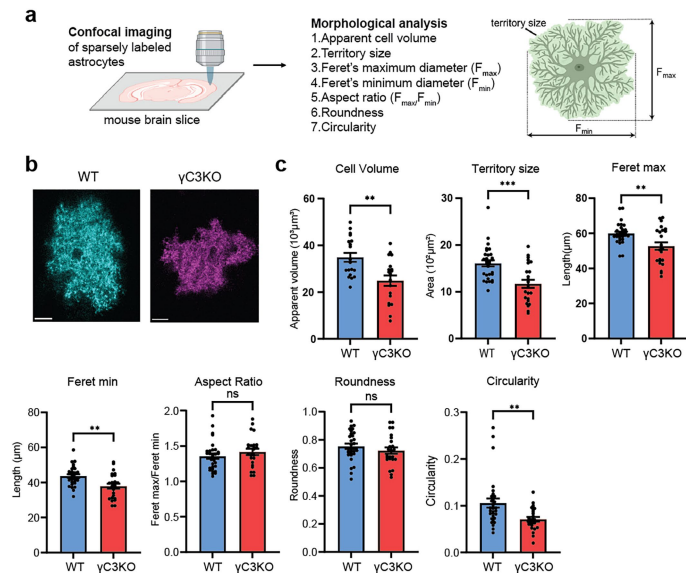
b, Astrocytes were labeled from P8 to P21 in the visual cortex, and tissues were subsequently stained with GFP antibodies. Representative images were obtained from three mice and have been routinely observed in injections with similar results.



Extended Data Fig. 2 | Identification of astrocyte γ C3 gene expression in V1.

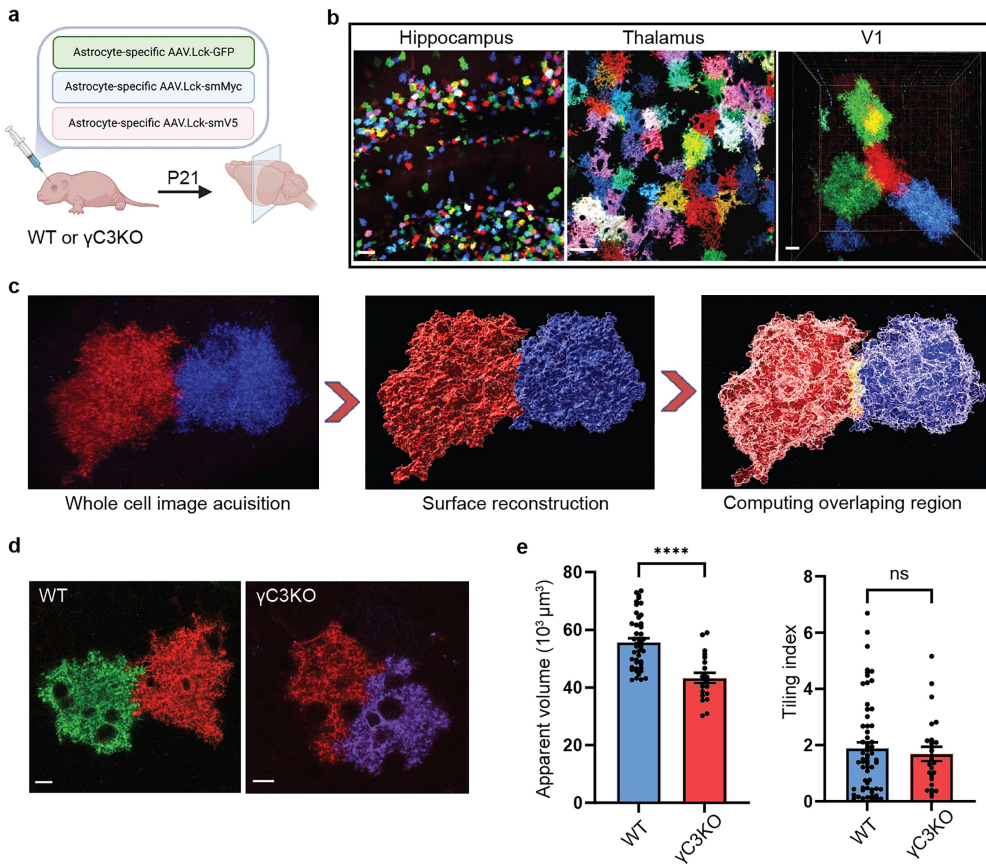
a, Low-magnification image illustrating γ C3 expression in astrocytes across both upper (L2/3) and lower (L5/6) cortical layers. γ C3 expression is also expressed in other cell types in these regions. Scale bar, 40 μ m. Representative images are from experiments quantified in (b), which were repeated independently in three mice. **b**, Astrocyte cell areas were segmented based on the expression of the astrocyte-specific marker *Slc1a3*, detected using an RNAscope *in situ* hybridization probe. γ C3 expression was detected using an isoform-specific RNA probe. Solid outlines indicate the cell boundaries of identified single astrocytes. γ C3 RNA puncta per cell were quantified within *Slc1a3*-positive

regions in layers 2/3 and 5/6 of V1 in WT mice at P21. N = 280 cells from three mice. Statistical comparisons were performed using the two-sided Wilcoxon rank-sum test, with nested analysis treating the animal as the unit of analysis. Error bars represent the standard error of the mean (s.e.m.). The probe specificity to γ C3 is supported by two observations. First, each of the multiple probes (referred to as Z probes) in the probe set is assessed computationally for cross-reactivity with non-cognate sequences in the transcriptome. Second, signal amplification requires adjacent Z probes to bind simultaneously, which contributes additional stringency in signal detection. Scale bar, 10 μ m.



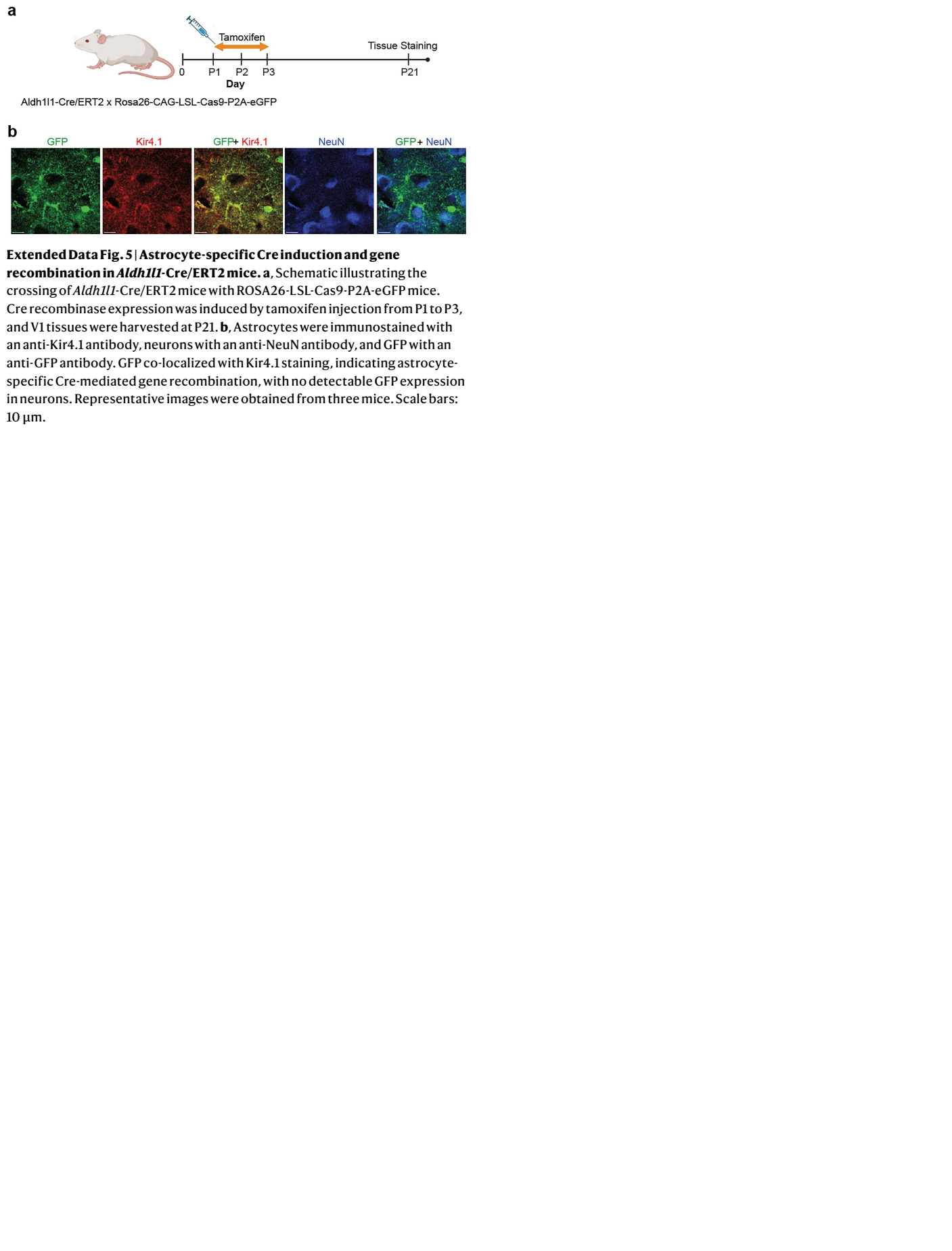
Extended Data Fig. 3 | Evaluating astrocyte morphology in the hippocampus

CA1 using multiple morphological metrics. **a**, To assess the morphological characteristics of astrocytes, we retro-orbitally injected WT or γ C3 KO mice with AAVs expressing Lck-smV5, Lck-smMyc, and Lck-GFP under the control of the astrocyte-specific *GfaABC1D* promoter. The mice were harvested at P21 and subjected to immunostaining with anti-Myc, anti-V5, and anti-GFP antibodies. Roundness: Measures how closely the shape's minor and major axes resemble a perfect circle. Circularity: Quantifies how similar the object's area and perimeter are to a perfect circle. **b**, Representative images of single astrocytes, flattened in a confocal volume, obtained from the CA1 hippocampus of both WT and γ C3 KO mice. Representative images were obtained from three mice. **c**, The results are summarized in plots representing various morphological parameters. Two-sided unpaired t-tests with Welch's correction was used to compare WT and γ C3 KO groups. Apparent cell volume: WT, n = 19 astrocytes from three mice; γ C3 KO, n = 19 astrocytes from three mice. Feret max, Feret min, aspect ratio, territory size, roundness, and circularity: WT, n = 30 astrocytes from three mice; γ C3 KO, n = 24 astrocytes from three mice. Error bars, s.e.m. Scale bars, 10 μm . **p < 0.01; ***p < 0.001. Nested analysis was performed for all statistical comparisons to confirm the results, and details are provided in Supplementary Table 4.

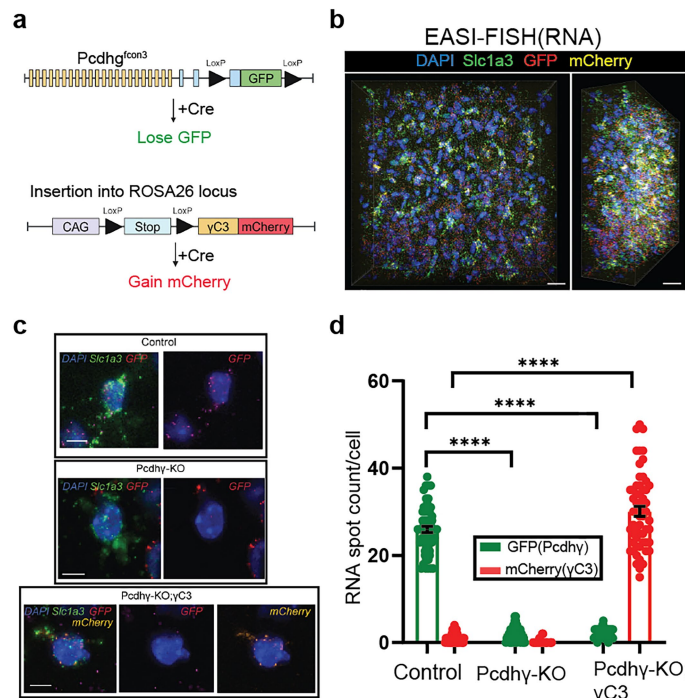


Extended Data Fig. 4 | Brain-wide multicolor labeling of astrocyte morphology. **a**, To enhance the labeling of fine astrocytic processes, smFPs were targeted to the plasma membrane using the Lck domain and packaged into AAV.PhP.eb serotype, which was delivered via the retroorbital route into P1 mice. Brains were harvested at P21. **b**, Multicolor labeling of astrocytes in the brain. WT mice were injected with AAV expressing Lck-smV5, Lck-smMyc, and Lck-GFP driven by the astrocyte-specific *GfaABC1D* promoter. Stochastic multicolor labeling of astrocytes is observed throughout the brain, including the hippocampus, thalamus, and visual cortex. The right panel shows a 3D reconstruction of neighboring astrocytes in layer 6 of V1. Scale bars 1 mm (hippocampus), 40 μm (thalamus), 10 μm (V1). **c**, Astrocyte volumes were

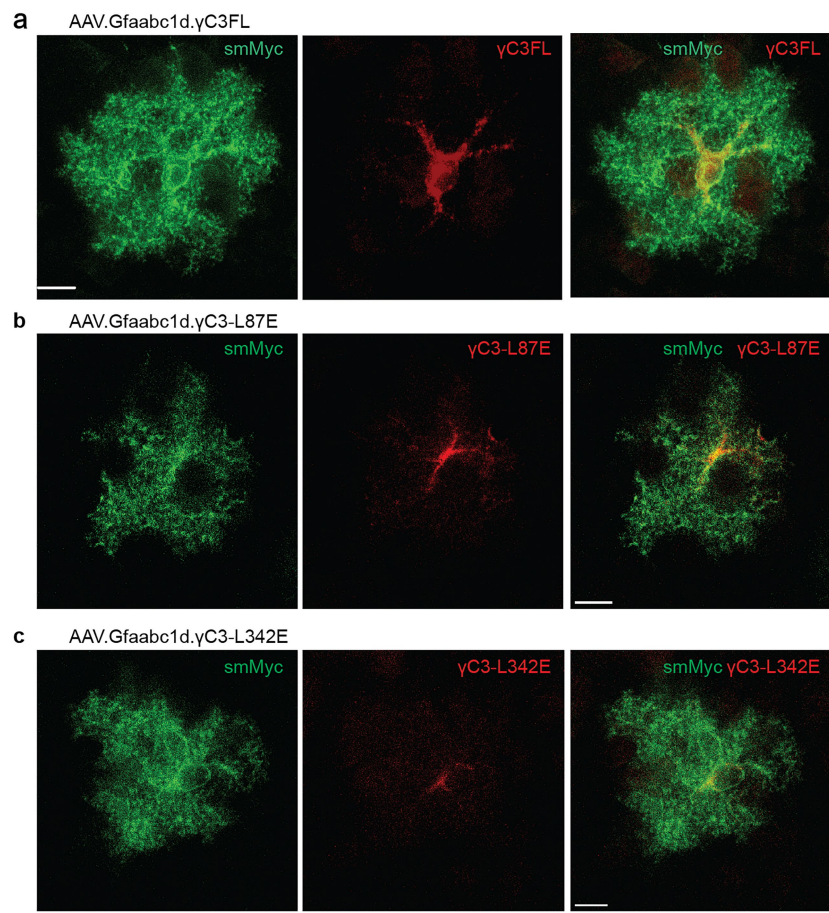
computed through surface reconstruction. The voxels inside each surface that overlap with each other were calculated and highlighted in yellow, generating a new surface from the overlapping regions. **d,e**, Astrocyte tiling index was calculated by dividing the overlapping volume between adjacent astrocytes by the volumes of a single astrocyte. Both WT and γ C3KO astrocytes exhibited minimal overlap with adjacent astrocytes. Two-sided unpaired t-tests with Welch's correction was used to compare WT and γ C3KO groups. WT, n = 44 astrocytes from three mice; γ C3KO, n = 21 astrocytes from three mice. Error bars, s.e.m. Scale bars 10 μm . ***p < 0.0001. Nested analysis was performed for all statistical comparisons to confirm the results, and details are provided in Supplementary Table 4.



Article

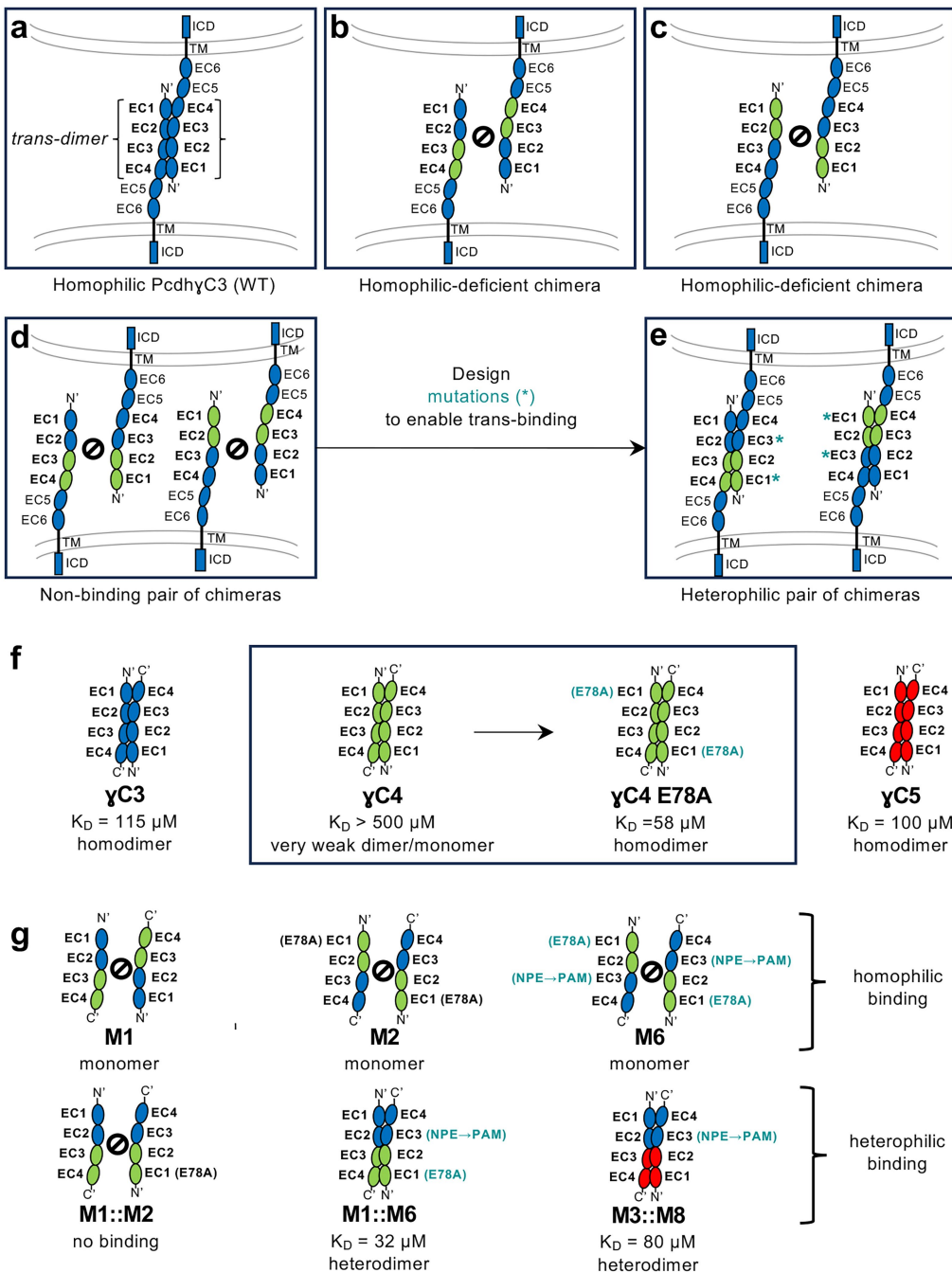


Extended Data Fig. 6 | Validation of astrocyte-specific Pcdhy KO and rescue of γC3 in cortical astrocytes. **a**, Diagrams of conditional Pcdhy KO and Cre-inducible γC3 alleles. Each Pcdhy protein is encoded by an mRNA comprising one of 22 variable exons (yellow) and the 3 constant “C” exons (blue). In the *Pcdhg^{con3}* KO allele, loxP sites flank the final constant exon, which is fused with GFP at the carboxy-terminus. Cre recombination results in loss of GFP-tagged Pcdhy proteins. In the ROSA26-CAG::lox-Stop-lox-γC3-mCherry Cre-inducible mice, Cre-mediated excision of the stop codon leads to the expression of γC3 with mCherry fused to the carboxy-terminus. In animals carrying both alleles and astrocyte-specific Cre, GFP is lost. As mCherry sequences are incorporated into the 3'-end of the γC3 mRNA, in the absence of Cre, the “Stop” cassette leads to transcription termination. Thus, mCherry containing transcripts are only seen upon excision of the “Stop” cassette. **b, c**, *In situ* detection of Pcdhy expression in visual cortex from whole-mount expanded tissues by EASI-FISH³⁴. **(b)** Low-magnification view, **(c)** High-magnification view of single optical sections from whole-mount preparations of the visual cortex from the indicated genotypes (see Methods). Upper panel: Control, Pcdhy/Pcdhy (GFP +). Middle panel: Pcdhy-KO, *Aldh1l1*-Cre/ERT2; Pcdhy/Pcdhy (GFP-). Lower panel: Pcdhy-KO;γC3, *Aldh1l1*-Cre/ERT2; Pcdhy/Pcdhy;γC3 (GFP- and mCherry +). Astrocytes were labeled with *Slc1a3* probes. **d**, Quantification of Cre-mediated recombination in astrocytes. RNA *in situ* hybridization confirmed efficient deletion of the Pcdhy genes in conditional KO mice. In control mice, GFP-tagged RNA from Pcdhy locus is expressed. In Pcdhy-KO mice, the GFP-tagged RNA is removed from the Pcdhy locus. In Pcdhy-KO;γC3 mice, the GFP-tagged RNA is removed, and the γC3 RNA transcript expressed from the ROSA26 locus is tagged with mCherry sequence. Note control and Pcdhy-KO do not contain the ROSA26-CAG::lox-Stop-lox-γC3-mCherry construct. Thus, the sparse mCherry puncta is non-specific hybridization. The Kruskal-Wallis test was used to compare the number of RNA puncta among the groups, followed by Dunn’s multiple comparison test for post-hoc pairwise comparisons. Specific p-values are provided in Supplementary Table 4. Control: n = 61 astrocytes from two mice; Pcdhy-KO, n = 58 astrocytes from three mice; Pcdhy-KO;γC3, n = 58 astrocytes from three mice. Error bars, s.e.m. Scale bars, 10 μm. ***p < 0.0001.



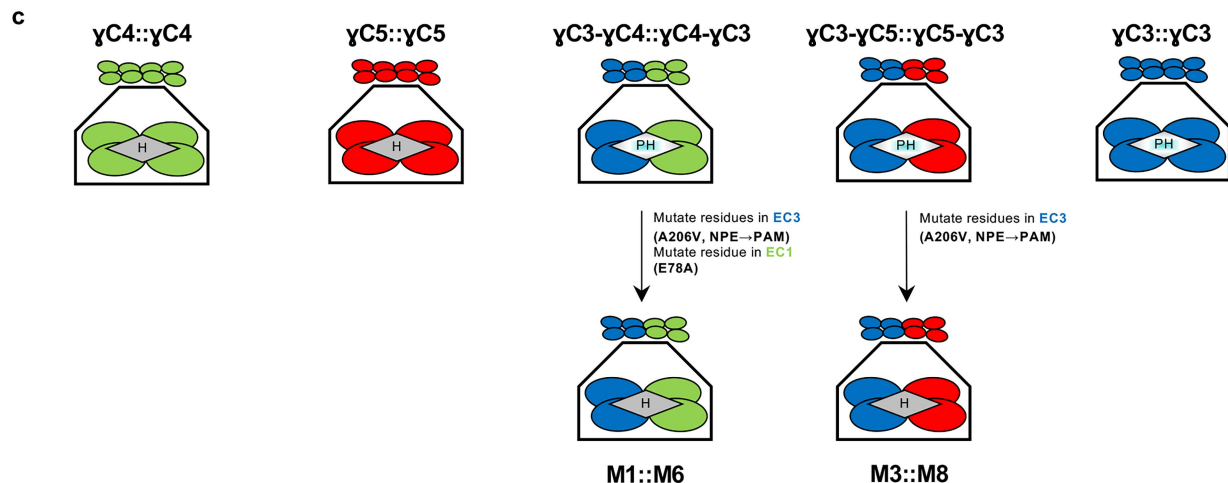
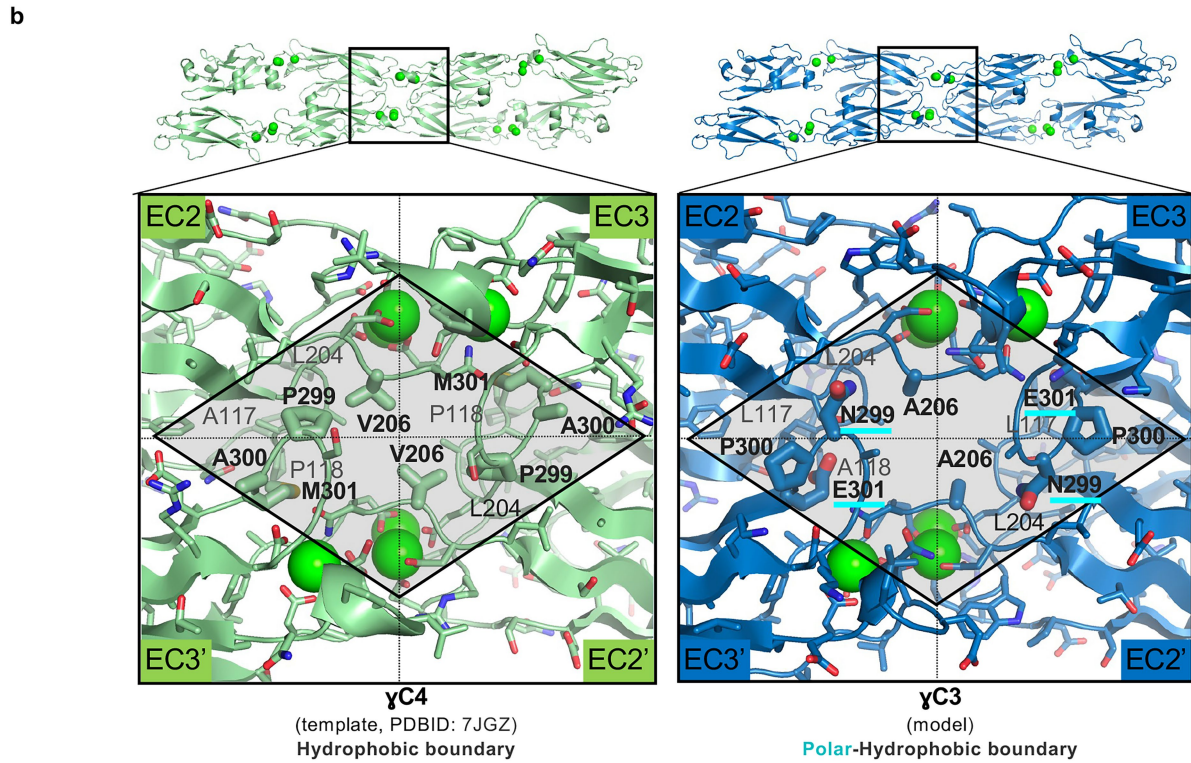
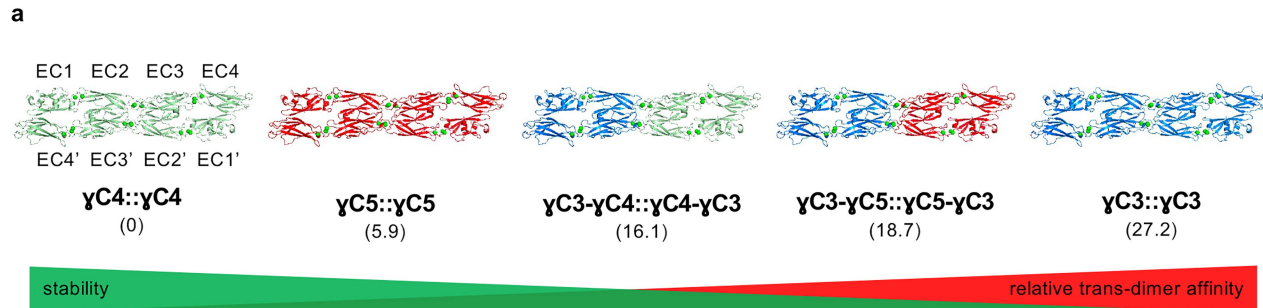
Extended Data Fig. 7 | Expression of AAVs expressing γ C3FL and γ C3 homophilic binding mutants in vivo. AAV.PhP.eB was used to express Lck-smMyc, γ C3 full-length (γ C3FL), γ C3-L87E, and γ C3-L342E mutants under an astrocyte-specific *GfaABC1D* promoter in γ C3 KO mice. AAV.PhP.eB expressing γ C3FL, γ C3-L87E, and γ C3-L342E, tagged with a C-terminal 3 \times V5, were retro-orbitally delivered into P1 mice. Astrocyte morphology was labeled by

co-injecting AAV.*GfaABC1D* expressing Lck-smMyc and visualized with an anti-Myc antibody (green). Expression of γ C3FL, γ C3-L87E, and γ C3-L342E was detected using an anti-V5 antibody (red). **a**, Expression of γ C3FL. Representative images were obtained from five mice. **b**, Expression of γ C3-L87E. Representative images were obtained from five mice. **c**, Expression of γ C3-L342E. Representative images were obtained from five mice. Scale Bars 10 μ m.



Extended Data Fig. 8 | Design of heterophilic protocadherin chimera pairs that lost homophilic binding. **a**, Contact between cell membranes (grey) of astrocyte sister branches (WT). $\gamma\text{C}3$ molecules (blue) forming a trans-dimer (in curly brackets) are shown schematically with extracellular cadherin (EC) domains as ellipses. **b,c**, Homophilic-deficient cPcdh chimeras. **d**, A pair of chimeras (one from **b** and another from **c**) co-expressed in the same astrocyte. **e**, A pair of chimeras in **d** modified with mutations (asterisk, cyan) that enable

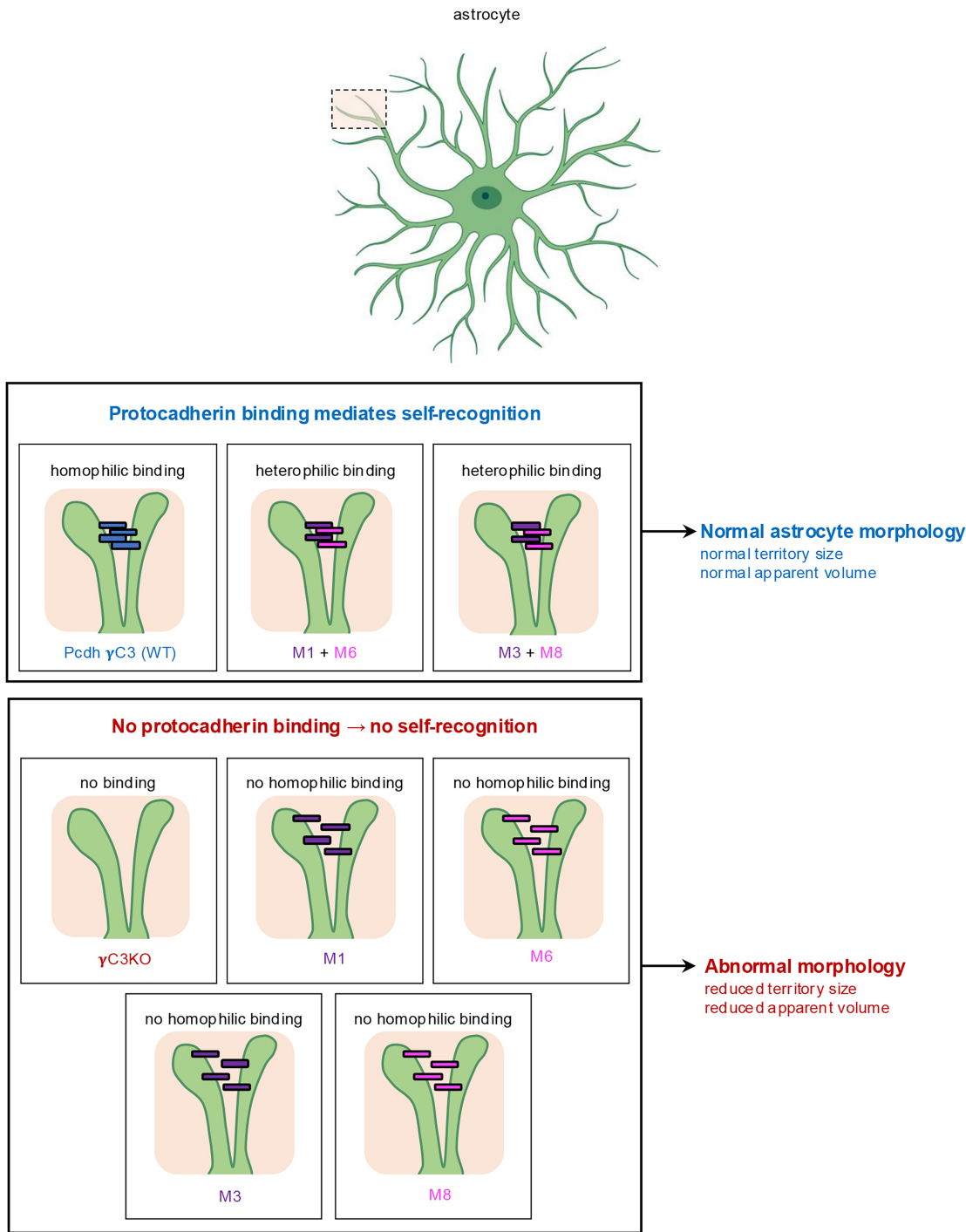
heterophilic binding. **f**, Summary of AUC experiments of WT $\gamma\text{C}3$, $\gamma\text{C}4$, and $\gamma\text{C}5$, parts of which were used for chimera design. Of note, AUC on $\gamma\text{C}5$ was done in the context of the EC1-EC5 fragment, but only the EC1-EC4 trans-dimer is shown in the schematic. **g**, Summary of AUC experiments on the designed chimeras. See Methods for details on mutation (cyan) design. A sign with a circle and a line through it depicts inability to form dimers.



Extended Data Fig. 9 | Trans-dimer models and their properties at the EC2-EC3 boundary. **a**, Relative FoldX energies (in parenthesis in kcal/mol) of the EC1-EC4'::EC4-EC1' trans-homodimers assuming all complexes form dimers identical in C α backbone to $\gamma\text{C}4::\gamma\text{C}4$. The chimeras are color-coded based on the sequence composition: $\gamma\text{C}3$ (blue), $\gamma\text{C}4$ (green) or $\gamma\text{C}5$ (red). All structures shown in ribbon representation with calcium atoms as green balls. **b**, Comparison of the amino acid properties at the EC2EC3 boundary of $\gamma\text{C}4$ trans-dimer and

$\gamma\text{C}3$. Protein backbone is in ribbon representation. Residues are shown as sticks in the expanded view of the EC2EC3::EC3'EC1' interface. Residues that differ in properties between $\gamma\text{C}4$ and $\gamma\text{C}3$ in a diamond-shaped area correspond to thicker sticks. Polar residues predicted to destabilize $\gamma\text{C}3$ trans-dimer in the $\gamma\text{C}4$ -like orientation are underlined in cyan. **c**, Schematic representation of the expanded views shown in **b** for all WT and chimera proteins. H – hydrophobic boundary, PH – polar/hydrophobic non-complementary boundary.

Article



Extended Data Fig. 10 | Summary of astrocyte self-recognition and morphogenesis via γ C3 and chimeric isoform binding. Astrocyte morphology relies on self-recognition mediated by γ C3. Binding between γ C3 proteins is likely to activate intracellular signaling pathways which specify distinct morphological consequences. Chimeras which have lost homophilic binding (e.g. M1, M6, M3, and M8) do not promote normal morphogenesis on their own. By contrast, pairs of complementary chimeras (e.g. M1 + M6 and M3 + M8) which bind heterophilically promote normal morphogenesis when expressed in the

same astrocyte. The precise mechanism by which γ C3 regulates morphogenesis is unclear. Binding could activate repulsion^{15,48}. The initial repulsive response may direct process extension away from sister branches and this would indirectly promote process outgrowth. Alternatively, transient binding between γ C3 on opposing processes may directly promote the assembly of signaling complexes which could promote process outgrowth^{25,44} (see Discussion).

Reporting Summary

Nature Portfolio wishes to improve the reproducibility of the work that we publish. This form provides structure for consistency and transparency in reporting. For further information on Nature Portfolio policies, see our [Editorial Policies](#) and the [Editorial Policy Checklist](#).

Statistics

For all statistical analyses, confirm that the following items are present in the figure legend, table legend, main text, or Methods section.

n/a Confirmed

- The exact sample size (n) for each experimental group/condition, given as a discrete number and unit of measurement
- A statement on whether measurements were taken from distinct samples or whether the same sample was measured repeatedly
- The statistical test(s) used AND whether they are one- or two-sided
Only common tests should be described solely by name; describe more complex techniques in the Methods section.
- A description of all covariates tested
- A description of any assumptions or corrections, such as tests of normality and adjustment for multiple comparisons
- A full description of the statistical parameters including central tendency (e.g. means) or other basic estimates (e.g. regression coefficient) AND variation (e.g. standard deviation) or associated estimates of uncertainty (e.g. confidence intervals)
- For null hypothesis testing, the test statistic (e.g. F , t , r) with confidence intervals, effect sizes, degrees of freedom and P value noted
Give P values as exact values whenever suitable.
- For Bayesian analysis, information on the choice of priors and Markov chain Monte Carlo settings
- For hierarchical and complex designs, identification of the appropriate level for tests and full reporting of outcomes
- Estimates of effect sizes (e.g. Cohen's d , Pearson's r), indicating how they were calculated

Our web collection on [statistics for biologists](#) contains articles on many of the points above.

Software and code

Policy information about [availability of computer code](#)

Data collection

Pcdh sequences of isoforms: Uniprot database; <https://www.uniprot.org>
Pcdh structures: RCSB Protein Data Bank; <https://www.rcsb.org>

Data analysis

Calculating effects of mutations on protein-protein binding: FoldX (version 4c); <https://foldxsuite.crg.eu>
Modeling heterophilic protocadherin chimeras: FoldX (version 4c); <https://foldxsuite.crg.eu>
Structure alignment and visualization: Pymol (Version 2.5.4); <https://www.pymol.org>
Multiple sequence alignment (MSA): Clustal Omega; <https://www.ebi.ac.uk/jDispatcher/msa/clustalo>
MSA visualization: ESPript 3.0; <https://escript.ibcp.fr/ESPript/ESPript/>
Solvent density and protein v-bar were determined using SednTerp (Alliance Protein Laboratories)
For calculation of dimeric Kd and apparent molecular weight, all useful data were used in a global fit, using SedPhat.
Statistical analyses were performed using GraphPad Prism version 10.3.1.
Confocal images were acquired by a Zeiss LSM 880 confocal microscope equipped with Zen digital imaging software
2D morphological analysis and quantification: ImageJ software.
Image segmentation and quantification in 3D: Imaris (version 10.01 Bitplane)

For manuscripts utilizing custom algorithms or software that are central to the research but not yet described in published literature, software must be made available to editors and reviewers. We strongly encourage code deposition in a community repository (e.g. GitHub). See the Nature Portfolio [guidelines for submitting code & software](#) for further information.

Data

Policy information about [availability of data](#)

All manuscripts must include a [data availability statement](#). This statement should provide the following information, where applicable:

- Accession codes, unique identifiers, or web links for publicly available datasets
- A description of any restrictions on data availability
- For clinical datasets or third party data, please ensure that the statement adheres to our [policy](#)

Data supporting the findings of this study are available in the main text and supplementary materials. Raw data for all animal studies and gene analysis have been provided in the supplementary files. The raw imaging data are not publicly available due to large file sizes but are available from the corresponding author upon reasonable request.

Research involving human participants, their data, or biological material

Policy information about studies with [human participants or human data](#). See also policy information about [sex, gender \(identity/presentation\), and sexual orientation](#) and [race, ethnicity and racism](#).

Reporting on sex and gender

N/A

Reporting on race, ethnicity, or other socially relevant groupings

N/A

Population characteristics

N/A

Recruitment

N/A

Ethics oversight

N/A

Note that full information on the approval of the study protocol must also be provided in the manuscript.

Field-specific reporting

Please select the one below that is the best fit for your research. If you are not sure, read the appropriate sections before making your selection.

Life sciences

Behavioural & social sciences

Ecological, evolutionary & environmental sciences

For a reference copy of the document with all sections, see nature.com/documents/nr-reporting-summary-flat.pdf

Life sciences study design

All studies must disclose on these points even when the disclosure is negative.

Sample size

Power analysis was conducted using values for power of 0.8 or higher and alpha of 0.1 or lower and an estimated effect size based on pilot data.

Data exclusions

No data was excluded from this manuscript

Replication

To verify the reproducibility of the experimental findings, all data collection was done in multiple batches comprising at least 3 replicates. The AUC protein binding experiments are representative of two technical replicates. All attempts at replication were successful.

Randomization

Experimental groups (cells, animals) were determined by genotype. The mice were randomly allocated to a group as they became available and of age from the breeding colony in alternation.

Blinding

For Pcdh chimera designs, we used prior-knowledge based analysis (relying on previously measured binding affinities and previously solved structures). We modeled complexes that had no solved structures using homology modeling and templates of available complexes. In the study of cell morphology, the mouse genotype was known during treatment and blinded during imaging collection. Data were not blinded for analysis because, in most experiments, the experimenter could visually recognize the mutant phenotype due to the clear alteration in cell morphology. The phenotype was quantified using standardized computational algorithms (detailed in the Methods) that were kept constant for all images.

Reporting for specific materials, systems and methods

We require information from authors about some types of materials, experimental systems and methods used in many studies. Here, indicate whether each material, system or method listed is relevant to your study. If you are not sure if a list item applies to your research, read the appropriate section before selecting a response.

Materials & experimental systems

n/a	Involved in the study
<input type="checkbox"/>	<input checked="" type="checkbox"/> Antibodies
<input type="checkbox"/>	<input checked="" type="checkbox"/> Eukaryotic cell lines
<input checked="" type="checkbox"/>	<input type="checkbox"/> Palaeontology and archaeology
<input type="checkbox"/>	<input checked="" type="checkbox"/> Animals and other organisms
<input checked="" type="checkbox"/>	<input type="checkbox"/> Clinical data
<input checked="" type="checkbox"/>	<input type="checkbox"/> Dual use research of concern
<input checked="" type="checkbox"/>	<input type="checkbox"/> Plants

Methods

n/a	Involved in the study
<input checked="" type="checkbox"/>	<input type="checkbox"/> ChIP-seq
<input checked="" type="checkbox"/>	<input type="checkbox"/> Flow cytometry
<input checked="" type="checkbox"/>	<input type="checkbox"/> MRI-based neuroimaging

Antibodies

Antibodies used

Rabbit anti-V5 (Bethyl A190-120A)
 Chicken anti-V5 (Bethyl A190-118A)
 Anti-c-myc rat antibody (Biorad JAC6)
 Anti-GFP antibody (Abcam ab290)
 Anti-NeuN (Millipore MAB377, clone A60)
 Anti-Kir4.1 (Alomone Labs APC-035)
 Alexa Fluor 488 goat anti-chicken (Invitrogen A-11039)
 Alexa Fluor 488 goat anti-rabbit (Invitrogen A-11008)
 Alexa Fluor 568 goat anti-Rat (Invitrogen A-11077)
 Alexa Fluor 568 goat anti-rabbit (Invitrogen A-11011)
 Alexa Fluor 647 goat anti-rabbit (Invitrogen A-21245)

Validation

The anti-GFP antibody (Abcam) is the standard antibody used in the field for labeling Green Fluorescent Protein (GFP). The NeuN antibody is a standard in the field as a neuronal marker. The antibodies used with smFP probes (Chicken anti-V5, Rabbit anti-V5, and Rat anti-c-myc), along with the corresponding secondary antibodies (Alexa Fluor 488 goat anti-chicken, Alexa Fluor 488 goat anti-rabbit, Alexa Fluor 568 goat anti-rat, Alexa Fluor 568 goat anti-rabbit, and Alexa Fluor 647 goat anti-rabbit) are validated in Nern et al., 2015; Viswanathan et al., 2015; and Veldman et al., 2020, as well as by our own work, as they consistently reproduce the known morphology of astrocytes and align with the morphology labeled by GFP-labeled astrocytes. The Kir4.1 antibody was validated using mouse knockout models by the manufacturer and is widely used in the astrocyte research community as an astrocyte marker. The Alexa Fluor-conjugated secondary antibodies were validated by Invitrogen using immunohistochemistry. Datasheets for all commercial antibodies are available on the manufacturers' websites.

Eukaryotic cell lines

Policy information about [cell lines and Sex and Gender in Research](#)

Cell line source(s)	human embryonic kidney Freestyle cells, HEK293F (Invitrogen)
Authentication	human embryonic kidney Freestyle cells, HEK293F (Invitrogen) used in this study were authenticated by morphology and PCR
Mycoplasma contamination	human embryonic kidney Freestyle cells, HEK293F (Invitrogen) used in this study were routinely tested and confirmed to be Mycoplasma negative.
Commonly misidentified lines (See ICLAC register)	No commonly misidentified cell lines were used in the study.

Animals and other research organisms

Policy information about [studies involving animals; ARRIVE guidelines](#) recommended for reporting animal research, and [Sex and Gender in Research](#)

Laboratory animals	Both male and female mice were used in alternating batches in C57BL/6N background. The study used mice at postnatal days P1, P2, P3, P7, P14 and P21. Pcdhyfcon3/fcon3 transgenic mice were generated by Josh Sanes at Harvard University; ROSA26-CAG::lox-Stop-lox-PcdhyC3-mCherry mice were generated by Julie Lefebvre and Joshua Sanes at Harvard University; and Aldh1l1-Cre/ERT2 (IMSR_JAX:031008) and ROSA26-LSL-Cas9-P2A-eGFP (IMSR_JAX:026175) mice were obtained from the Jackson Laboratory. Mice were housed at the University of California, Los Angeles, under standard conditions in accordance with UCLA's Animal Care and Use Committee protocol number 2009-031-31A. Animals were maintained at ambient temperature and humidity with a 12-hour light/dark cycle. Mice had ad libitum access to food and water with up to four adult animals per cage.
Wild animals	The study did not involve wild animals.
Reporting on sex	Both male and female mice were used in alternating batches.
Field-collected samples	The study did not use field-collected samples

Ethics oversight

All experiments were conducted in accordance with the National Institute of Health (NIH) Guide for the Care and Use of Laboratory Animals and were approved and overseen by the Chancellor's Animal Research Committee (ARC) at the University of California, Los Angeles (UCLA).

Note that full information on the approval of the study protocol must also be provided in the manuscript.

Plants

Seed stocks

N/A

Novel plant genotypes

N/A

Authentication

N/A